Distributed Biological Observatory Region 1:
Physics, chemistry and plankton in the northern Bering Sea

Phyllis J. Stabeno[1*], Shaun W. Bell[1,2], Nicholas A. Bond[1,2], David G. Kimmel[3], Calvin W. Mordy[1,2], Margaret E. Sullivan[1,2]

[1]NOAA Pacific Marine Environmental Laboratory
7600 Sand Point Way NE
Seattle WA 98115-0070
Phone: (206) 526-6453
Fax: (206) 526-6485
Phyllis.stabeno@noaa.gov

[2] University of Washington/JISAO,
Seattle, WA 98105

[3] NOAA Alaska Fisheries Science Center
7600 Sand Point Way NE
Seattle WA 98115-0070

*Corresponding author

For submission to DSR-II

May 1, 2018
Revised: August 20, 2018
Revised: October 1, 2018
Revised: Nov 1, 2018

Abstract

Historically, the northern Bering Sea has been largely ice covered for 5-6 months each year. From 1980 to 2014, there was considerable variability in the timing of ice arrival and retreat, but there was no significant trend in these variables. During three of the last four years (2014-2015, 2016-2017, 2017-2018) ice has arrived later and retreated earlier, resulting in a shorter ice season. These changes may be related to the delayed arrival of sea ice in the Chukchi Sea, under the paradigm that the Chukchi Sea freezes before the northern Bering Sea. Under such a sequence of events, the continued delay in arrival of sea ice in the Chukchi Sea will in turn delay the arrival of ice in the northern (and hence southern) Bering Sea; thus, past predictions that the northern Bering Sea will remain cold for the foreseeable future may be in question. In the northern Bering Sea, periods of 10-15 years with extensive ice in December and January are interrupted by shorter periods (2-5 years) of less extensive ice cover. The periods of low ice cover in December and January in the northern Bering Sea tend to coincide with periods of low ice cover in March and April in the southern Bering Sea. Sea ice impacts the marine ecosystem in multiple ways: early retreat of sea ice is correlated with warmer sea surface temperatures in the summer; delayed arrival of sea ice results in warmer bottom temperatures in fall and winter; multiple, consecutive years of extensive ice appear to be related to decreasing salinity and nutrients (nitrate and phosphate); and the timing of ice retreat influences the life cycle of *Calanus* spp. as warmer waters increase their development rate.

1. Introduction

Region 1 of the Distributed Biological Observatory (DBO-1) is an area of enhanced benthic productivity. It lies to the west of St. Lawrence Island on the Bering Sea shelf and is the southernmost of the DBO regions. DBO-1 is bounded by a 190 km × 200 km box, centered at 62.81°N, 174.11°W (Fig. 1). Within the region are 10 primary observing stations for shipboard sampling stretching from 62.01°N, 175.06°W to 63.60 °N, 172.59°W, and one long-term (2005–present) mooring (M8) located in the southwestern quadrant of the box at 62.194°N, 174.688°W.

Historically, the northern Bering Sea shelf has been largely ice covered from November through May (Stabeno et al., 2012a). The departure of ice in May is primarily through ice melt, which introduces low salinity water into the near surface region. In water deeper than ~50 m, the relatively weak winds in May cannot mix the entire water column, resulting in a surface lens of low salinity (~30) water overlaying the more saline (~32) bottom water. Thus, the part of DBO-1 with water depth greater than 50 m has a two-layer structure from June through September—a surface wind-mixed layer (~20 m deep) and a bottom tidally mixed layer (~30 m deep) separated by a pycnocline. Salinity and temperature contribute equally to the density stratification, which is twice as strong as observed on the southern portion of the shelf (Stabeno et al., 2012a). Mooring M8 is deployed in this two-layer structure.

Currents vary spatially in the DBO-1 region (Fig. 1; Kinder et al., 1986; Danielson et al., 2012). The northern portion is influenced by the Anadyr Current which flows northward and eastward along the coast of Siberia. While the Anadyr Current usually continues northward between St. Lawrence Island and the Siberian coast, entering the

Chukchi Sea through Bering Strait, the current is sometimes observed south of St. Lawrence Island. The mean flow in the southern part of DBO-1 is weaker and less organized. The northward flow along the 100-m isobath sometimes impinges on M8, but more often it flows west of the mooring, joining the Anadyr Current (Stabeno et al., 2016). Tidal currents are moderate at M8 (e.g., major axis of tidal ellipse for M_8 is ~12 cm s^{-1}), which allows a shallower bottom mixed layer and a thicker pycnocline than is observed on the southern Bering Sea shelf, where tidal currents are almost twice as strong (Stabeno et al., 2010).

While the southern Bering Sea shelf was predicted to warm, the northern shelf was predicted to remain cold for the foreseeable future, with extensive sea ice during winter and early spring (Stabeno et al., 2012a; Wang and Overland, 2009). This is a result of multiple factors, including: in the northern Bering Sea, the sun is above the horizon for only a few hours during the late fall and early winter; the northern Bering Sea is surrounded by land—Siberia to the north and west, and Alaska to the east; and the relatively weak northward flow limits the transport of heat from the southern shelf.

Observations indicate that there has been a decrease in biomass (e.g., reduction in the dominant bivalve community) and reduced carbon supply to the sea floor (Grebmeier et al., 2006; Grebmeier, 2012). Our study focuses on DBO-1 and explores some of the changes to lower trophic levels (physics, chemistry, and zooplankton) in the northern Bering Sea that may contribute to the apparent decrease in benthic production. We begin by examining changes in the temporal and spatial variability in sea-ice extent, since it is a key physical driver in determining ocean temperature, timing of primary production and trophic interactions (Sigler et al., 2014; Stabeno et al., 2010, 2012b; Hunt et al., 2011).

We use self-organized maps (SOMs) to explore the timing and pattern of sea-ice arrival in the northern Bering Sea. This type of analysis, which is becoming more common for meteorological and oceanographic applications (e.g., Liu and Weisberg, 2011), reduces (clusters) large data sets of maps into a small set of patterns. Sea-ice variability is then related to ocean temperature, salinity, nutrients, and zooplankton.

2. Data sources and methods

2.1 Atmospheric variables

The National Center for Environmental Prediction (NCEP) – Department of Energy (DOE) Reanalysis uses a state-of-the-art analysis/forecast system to perform data assimilation on a 2.5° latitude by 2.5° longitude grid with data ranging from January 1979 to August 2017 (Kalnay et al., 1996; Kanamitsu et al., 2002). Mean-daily sea level pressure (SLP) distributions were constructed from the NCEP/DOE Reanalysis II product and interpolated to the desired grid points bounded by 180–155 °W, 52–72.5 °N. NCEP Reanalysis data were obtained from the NOAA Earth System Research Laboratory, Physical Sciences Division in Boulder, Colorado, USA (http://www.esrl.noaa.gov/psd/.

2.2 Sea ice

Sea-ice concentration data were retrieved from two sources. The first is the daily (every other day prior to 1987) Version 3 bootstrap Sea-Ice Concentrations from Nimbus-7 SMMR (Scanning Multichannel Microwave Radiometer) and DMSP SSM/I-SSMIS (Defense Meteorological Satellite Program, Special Sensor Microwave/Image Sounder), which is available from the National Snow and Ice Data Center (NSIDC;

http://nsidc.org/data/nsidc-0079) and uses NASA's Earth Observing System AMSR-E (Advanced Microwave Scanning Radiometer for EOS) bootstrap algorithm. This data set covers the period of 16 October 1978 – 31 March 2017 and is periodically updated as new data become available (Comiso, 2017). The second source is Version 1 Near-Real-Time (NRT) DMSP SSMIS Daily, and is also available from NSIDC (http://nsidc.org/data/nsidc-0081). Although designed to match the bootstrap processing of Version 3 as much as possible, the derivation of the Version 1 product is limited to a short window (within 24 hours of data acquisition) and whatever data and algorithms are available at the time of processing (Maslanik and Stroeve, 1999). Data from the NRT algorithms are available from 2015-present and are used in this paper to extend our analysis through the 2017/2018 winter season.

2.3 Moorings

The biophysical moorings deployed at site M8 are subsurface moorings, typically recovered and redeployed in September for year-long data collection. Moorings have been maintained at the M8 site since 2005. The depths of the shallowest instruments on the main moorings were ~20 m, to avoid deep ice keels. In three of the years, an additional subsurface mooring was deployed in July and recovered in September, providing measurements in the upper 20 m of the water column.

Typically, data collected by instruments on the moorings included temperature (miniature temperature recorders, SeaBird SBE-37, SBE-39 and SBE-16), salinity (SBE-37 and SBE-16), and chlorophyll fluorescence (WET Labs DLSB ECO fluorometer). Currents were measured using an upward-looking, bottom-mounted, 300 or 600 kHz

Teledyne RD Instruments acoustic Doppler current profiler (ADCP) deployed next to the main mooring. All instruments were calibrated prior to deployment. Each year, the main mooring is constructed of heavy chain to help protect the instruments and buoy from loss due to sea ice. Sampling intervals varied among the different instruments and ranged from every 10 minutes to once per hour.

In 2016 an ASL Environmental Sciences IPS5 upward-looking sonar ice profiler with an operating frequency of 420 kHz and a 1.8° beam width was deployed on a separate mooring at site M8. The instrument recorded range and amplitude data every second, and sensor data (temperature and pressure) every minute. Data processing, including de-spiking and null-target recovery, was performed using ASL Matlab-based software. Raw range data were corrected for mooring tilt, and pressure data were corrected for atmospheric pressure using NCEP North American Regional Reanalysis (NARR) 3-hourly SLP data. Water level was calculated using IPS5 water pressure and atmospheric pressure. Ice draft (keel depth) was then calculated using corrected range, pressure and water-level data. The resulting ice draft data were visually inspected, and outliers were removed from the time series. Basic statistics were calculated in the Matlab environment.

All instruments were calibrated prior to deployment. The data were processed according to manufacturers' specifications. All current meter time series were low-pass filtered with a 35-hr, cosine-squared, tapered Lanczos filter to remove tidal and higher-frequency variability, and re-sampled at 6-hour intervals.

2.4 Hydrography and nutrients

Conductivity-temperature-depth (CTD) measurements were collected with a Seabird SBE 911plus system with dual temperature and conductivity (salinity), oxygen (SBE-43), photosynthetically active radiation (PAR; Biospherical Instruments QSP-200 L4S or QSP-2300), and chlorophyll fluorescence (WET Labs WETStar WS3S or WET Labs EcoFluorometer) sensors. Data were recorded during the downcast, with a descent rate of 15 m min^{-1} to a depth of ~35 m, and 30 m min^{-1} below that. Salinity calibration samples were collected on the up-cast on approximately half the casts and analyzed using a laboratory salinometer. Oxygen samples were taken on most casts and titrated at sea using the Winkler method.

Samples for dissolved inorganic nutrients (nitrate, nitrite, ammonium, phosphate, and silicic acid) were syringe filtered using 0.45 μm cellulose acetate membranes, and collected in 30-ml, acid-washed, high-density polyethylene bottles after three rinses. Samples were either analyzed on board, or were frozen and brought back to the laboratory for analysis. Prior experience demonstrates that nutrient concentrations are stable upon filtering and freezing (Dore et al., 1996; Mordy et al., 2012, Eisner et al., 2016).

Nutrients were determined on a customized autoanalyzer using a combination of analytical components from Alpkem, Perstorp, and Technicon. WOCE-JGOFS standardization and analysis procedures specified by Gordon et al. (1993) were closely followed including reagent preparation, calibration of labware, preparation of primary and secondary standards, and corrections for blanks and refractive index. Ammonium was measured using an indophenol blue method modified from Mantoura and Woodward

(1983). Silicic acid was measured immediately after thawing, and several days later to account for polymerization during freezing (Macdonald et al., 1986).

2.5 Zooplankton

Zooplankton were collected between August and October from 2005 to 2015 (excluding 2011 and 2013) from a 70-km^2 box around mooring location M8. Zooplankton were collected using oblique tows of paired bongo nets (20-cm frame with 153-μm mesh and a 60-cm frame with 333-μm mesh) (Napp et al., 2002) until 2012. After 2012, the 60-cm net was switched to 505-μm mesh. We believe the change in mesh size does not impact our interpretation of results based on the size range of copepodites stages of *Calanus marshallae*, reported as 0.9 to 2.9 mm for C2 to C6 stages (Liu and Hopcroft, 2007). The tows sampled the whole water column to within 5-10 m of the bottom depending on sea state. Net depth was determined in real time using a SBE-19 or SBE-49 CTD sensor (Sea Bird Electronics). The volume of water filtered was estimated using a General Oceanics flowmeter mounted inside the mouth of each net. Samples were preserved in 5% buffered formalin/seawater. Copepods were identified to the lowest taxonomic level and stage possible at the Zakład Sortowania i Oznaczania Planktonu (ZSIOP; Szczecin, Poland), and verified at the Alaska Fisheries Science Center, Seattle, Washington, USA. We enumerated *Calanus* spp. stage C1 and C2 from the 153-μm mesh net and stages C3-C6 from the 333/505-μm mesh net. It is important to note that while we report *Calanus* spp. as a mixture of *C. marshallae* and *C. glacialis*, the exact proportion of each species in the Bering Sea is unknown as these species are difficult to distinguish (Campbell et al., 2016). Throughout the paper, we refer to this mixture as *Calanus* spp.

2.6 Self-Organizing Maps

For the supervised SOM analysis, we used the R statistical software, Kohonen package (v3.0.4; Wehrens, 2015). Using bootstrap sea-ice concentration (see section 2.2) beginning in the 1979/80 winter season and ending in the 2016/2017 winter season, we averaged the data set into eight, 8-day periods in December and January. Mean SLP for the leading 8-day map was obtained and averaged from NCEP/DOE Reanalysis II. A grid representation is presented in Fig. 2 of the two fields used.

SLP is used to characterize the atmospheric forcing for two reasons. First and foremost, the distribution of SLP closely corresponds with that of the winds. On the temporal and spatial scales considered here, the wind spirals outward in a clockwise sense around high SLP centers and inward in a counter-clockwise sense around low SLP centers. The strength of the spatial gradient in SLP is approximately proportional to the speed of the wind. Second, patterns of anomalous SLP have long been used to characterize the state of the regional atmospheric circulation (e.g., Rodionov et al., 2007). In general, the SLP can be used to infer important aspects of the atmospheric forcing of the ocean.

The construction of SOMs entails making choices. With a goal of describing the co-variability of ice concentration and large-scale atmospheric forcing as characterized by SLP patterns, we carried out SOM analyses considering these two variables in tandem.

Because our primary interest is the ice concentration distributions, we weighted it heavier (70%) than the SLP (30%) in the multivariate SOM. The fraction ice concentration was scaled to range from 0 to 1, the SLP was demeaned and normalized to be between -1 and 1. Rescaled, but still demeaned, SLP patterns from the SOM “map” analysis are referred to as SLP anomalies (SLPA). In order to provide better geographical context, these “maps” are reverted back to geospatial representation such that the mean and anomalous state of each pattern is presented. Other parameters of the SOM analysis were set following suggestions in Liu and Weisberg (2011) and the papers referenced therein.

The preparation of SOMs also involves selection of the number of modes and their relationships to one another. A greater number of modes serve to more fully represent the range of possible states of a system, but can yield results that are less robust and with smaller distinctions between individual categories, complicating physical interpretations of the results. In addition, the “geometry” of SOM mappings influences the results, since neighboring modes share information from the input data. We examined SOM results for four different mappings: 3×3, 4×2, 4×3, and 6×3. The spatial patterns in the 3×3 and 4×2 mappings were very similar. The 4×3 mapping resulted in ice distributions that were similar to those in a 3×3 mapping, with several ice distributions that resembled one another, but associated with different SLP distributions. The 6×3 mapping provided more detailed spatial patterns, naturally, but with fewer individual cases per mode. We ultimately chose a 4×3 mapping (12 modes) to capture the most common ice concentration patterns (and in some cases their distinctively different SLP patterns) and to avoid consideration of rare states that are less likely to be truly characteristic of the system.

2.7 *Multi-scale Ultra-high Resolution SST (MUR)*

The Multi-scale Ultra-high Resolution SST product (MUR) is 0.01° latitude × 0.01° longitude daily sea surface temperature (SST) product available for June 2002 to present. This product was created by NASA's Jet Propulsion Laboratory (JPL, current version 4.1 http://dx.doi.org/10.5067/GHGMR-4FJ04) and is one of the highest resolution SST analyses available. It ingests MODIS/AVHRR/Microwave and in-situ data, and it is designed with high-resolution satellite datasets in mind. It uses the Multi-Resolution Variational Analysis method to integrate sensors and data with multiple timescales and aims to capture the evolution of sub-mesoscale features (Chin et al., 2017).

3. Results and Discussion

3.1 *Areal patterns of sea ice*

The timing of arrival and retreat of sea ice over the last 37 years (1981–2017) is examined within a 50 km × 50 km box centered on M8 (Fig. 3). Sea ice has arrived (defined as >20% areal coverage) as early as 30 November (in 1987) and as late as February 12 (in 2017), with an average arrival date of 27 December; sea ice retreated (areal concentration falls and remains below 20%) as early as 20 April (in 2016) and as late as 6 June (in 1999) with an average retreat date of 16 May. It is noteworthy that sea ice occurred in the M8 box in winter/spring 2018 on only two occasions: 4–8 February when it never exceeded 6% areal coverage and again on 14–20 March when it reached a maximum of almost 18% for a single day (17 March). These estimates of areal ice cover for 2017-2018 were calculated using the preliminary "real-time" data set, not the final bootstrap concentrations. Excluding 2017-2018, the average duration of sea ice in the M8 box is 141.9 ± 4.1 (mean ± standard error of the mean [SEM]) days.

From 1981 through 2014, there was no trend in the timing of sea-ice arrival, retreat nor duration. If the last three years (2015–2017) are included, however, the 37-year time series (1981–2017) has a significant trend with the date of arrival delaying by 0.76 days per year ($p=0.05$), date of retreat becoming earlier by 0.45 days per year ($p=0.03$), and duration decreasing by 0.75 days per year ($p=0.05$). The timing of ice arrival and retreat are not correlated. Approximately 80% of the variability in duration of ice at M8 results from variability in timing of ice arrival, which is not surprising since variability (standard deviation) in date of ice arrival is almost twice as large as the variability in date of ice retreat.

In sharp contrast to M8, the Chukchi Sea has been undergoing significantly later ice arrivals and earlier retreats for over two decades, combining to produce a significant expansion of the open water season (Serreze et al., 2016; Wood et al., 2015). The delay in the arrival time each year was twice as large as the accelerated time of retreat (Serreze et al., 2016). We examined sea ice in the southern Chukchi Sea (Fig. 2; area outlined by the dotted purple line), and defined the region as ice covered when the areal ice concentration exceeded 80% (orange line in Fig. 4). The trend (1981–2018) in the date of ice arrival in the southern Chukchi Sea was 0.7 days later per year ($p<0.001$), which is less than was observed by Serreze et al. (2016) for the entire Chukchi Sea.

From 1980 to 2017, the average date on which the southern Chukchi Sea froze (>80% areal ice cover) was 28 November, which is 28.6 ± 2.8 (SEM) days before the average date of ice arrival (20% areal ice cover) in the region around M8 (27 December). The timing between the freezing of the southern Chukchi and the area around M8 varied between 6 days (2007/2008) and 82 days (1983/1984). The two series are correlated ($r = 0.53$, $p<0.01$), but if the years after 2014 are excluded the two series are no longer significantly correlated (Fig. 4).

Several lines of evidence support the hypothesis that the northern Bering Sea freezes later than the southern Chukchi Sea (excluding shallow near-shore areas). First, using data from Met Office Hadley Centre, EN4, ocean temperatures in an area around M8 (175°W – 173°W, 61.5°N – 62.5°N) and an area around Chukchi Sea (170°W – 167°W, 67°N – 68°N) are compared. During summer, depth averaged temperatures in the upper 40 m near M8 are warmer than those in the southern Chukchi Sea. For instance, the mean (1990-2005) depth-averaged temperature for the July is 0.8°C warmer around M8 (4.0 ± 0.3) than it is the southern Chukchi Sea (3.2 ± 0.2). This heat must be lost to the atmosphere, before freeze-up can occur. Second, the average (1980-2011) daily net surface heat flux (European Centre for Medium-Range Weather Forecasts [ECMWF] ocean reanalysis ORA-S3) in the southern Chukchi changes sign (ocean begins losing heat to the atmosphere) in mid-August, approximately two weeks before the change occurs at M8. In August through October, the air-sea heat flux around M8 is ~50 watts m^{-2} greater (i.e., less heat lost from the ocean) than it is in the southern Chukchi Sea. In addition to the first two items, the heat flux over open water in the Chukchi Sea tends to result in warmer local air temperatures. Since the winds that form ice in fall/winter in the northern Bering Sea usually include a component from the north, a lack of sea ice in the

Chukchi Sea can result in the atmosphere being less conducive to forming ice in the northern Bering Sea.

This pattern of the Bering Sea freezing later than the Chukchi Sea has persisted for >40 years (Fig. 4) and there is no expectation that the physical mechanisms that support it will change. Freeze-up in the southern Chukchi Sea is trending later by ~0.7 days each year and the expected date of freeze-up in 2018 is within ~10 days of December 24, which is the average date of ice arrival at M8 from 1981-2014. (We use 1981-2014 here, because that is the period in which there was no significant trend in the timing of ice arrival.) If these patterns hold it can expected that the arrival of sea ice in the northern Bering Sea will be forced to trend later in future years.

It is unclear if the marked decrease in ice duration during three (2014/2015, 2016/2017, and 2017/2018) of the last four years is a harbinger of a new ice regime or just variability in the system. Such variability is not unheard-of. From 2002 to 2004 (Fig. 3c), there was decrease in ice duration of ~50 days, but during each of following 8 years ice duration was at or above average. Certainly, sea-ice extent during this last winter (2017/2018) was well beyond the range of anything previously observed. Arguably, the relatively warm ocean conditions in the Chukchi Sea in summer 2017 and the associated late freeze up (Wood et al., 2018) delayed ice formation in the Bering Sea. When ice began to appear in the vicinity of M8 in January it was interrupted by the strong wind anomalies out of the south in February (https://www.esrl.noaa.gov/psd/cgi-bin/data/composites/printpage.pl), which prevented extensive ice formation in the Bering Sea before March. In addition, relatively warm ocean temperatures in the Bering Sea can contribute to the delay in the advance of sea ice (Stabeno et al., 2010), and ocean temperatures in late winter 2018 were above average. It can be argued that the Chukchi will continue to freeze later and so delay the arrival of ice in the northern Bering Sea, but strong frigid winds from the northwest (which are common in the winter) can drive ice quickly over the shelf.

Since the period of ice advance typically occurs in December and January, we wanted to examine the spatial patterns of sea ice in more detail. Eight maps of average areal ice cover for 8-day periods were calculated (1–8 December, 9–16 December, 17–24 December, etc.). The spatial pattern of sea-ice cover in the northern Bering Sea shows ice typically arriving in the northeast and expanding toward the south and southwest (Fig. 5). Ignoring the southwest corner of each panel, which is over the basin, the northern Bering Sea shelf, on average, was ice covered by mid-January.

3.2 Self-Organizing Maps analysis: Sea ice and sea level pressure

Our objective herein is to examine the evolution of distributions of sea-ice concentrations, and how these changes co-vary with the regional atmospheric forcing as characterized by SLP. Ice concentration data from the bootstrap sea-ice product described in section 2.2 were averaged into eight periods of 8 days duration each for the months of December and January beginning with the 1979/1980 winter season and ending with the 2016/2017 winter season. For the same set of 8-day periods, mean SLP distributions were constructed from the NCEP/DOE Reanalysis II product. In our analysis of the co-variability between sea-ice concentrations and SLP, we focus on the SLP for the 8-day period preceding that for the sea-ice concentration. This length of lag between the forcing and sea-ice response appeared to yield the most consistent and sensible results. A gridded representation of the two fields is presented in Fig. 2.

We use SOM to describe the behavior of ice concentration distributions during the months of December and January in the northern Bering Sea. The SOM framework represents a type of unsupervised neural network and is being increasingly employed for meteorological and oceanographic applications (Liu and Weisberg, 2011). It has been found to be a useful tool for classifying and visualizing geophysical information through the clustering of large and complex data sets into a small set of modes that resemble the input patterns. In many applications, it has some advantages over other analysis methods such as principal component analysis (PCA). In particular, it can be effective in terms of representing the full continuum of a data set through its ability to catalog a combination of both common patterns and other states that are more rare but distinct. In an application akin to the present analysis, Cassano et al. (2016) used SOMs to characterize atmospheric circulation patterns associated with temperature extremes in Alaska during winter.

3.2.1 Individual patterns

To examine the period of freeze-up in more detail, SOM techniques are utilized to derive characteristic patterns of ice arrival from December 1979 to January 2017. This analysis was done using the same set of 8-day periods used to examine average sea-ice cover (Fig. 5), and was coupled with SLPA. The resulting analysis provided 12 sea-ice patterns (Fig. 6) and 12 related SLPA patterns, which were transformed to SLP (Fig. 7). To integrate atmospheric forcing with patterns of ice coverage, the average ice maps were associated with SLPA from the previous 8 days. For instance, the first 8-day period for sea ice was 1–8 December and the associated the SLPA map would be 23-30 November. The sea-ice maps were weighted at 70% and the normalized SLPA weighted at 30%.

The 12 patterns represent a total of 304 separate 8-day maps. The number of individual maps used to obtain each pattern (or the count) is indicated in the upper right-hand corner of the panels in Fig. 6. Pattern 3 (little or no ice) was the most common pattern (representing 48 individual, 8-day maps) and pattern 12 was the second most common (33 individual maps). The lowest number of counts (14) was pattern 10, which represented the most extensive ice.

The sea-ice patterns vary from almost no ice (pattern 3 in Fig. 6) to complete ice cover except in the southwest corner over the basin (pattern 10 in Fig. 6). The panels are color coded in shades of gray, going from white (pattern 3) to black (pattern 10) and are mapped onto a timeline (Fig. 8). Typically, ice occurs in higher concentrations in the east or northeast, and progresses southwestward with time. The exception to this is pattern 6 (yellow, Fig. 6). Here, the ice occurs mainly in the northern part of the study area.

Associated with each ice pattern (Fig. 6) is a SLP pattern (Fig. 7). Some of the ice patterns are similar (e.g., patterns: 4 and 5; 7 and 8; and 11 and 12), but they are associated with different SLP patterns during the previous 8 days. The groups in the left column of Fig. 7 (patterns 1, 4, 7, and 10) represent periods of higher SLP and the groups in the right column (patterns 3, 6, 9, and 12) represent periods of lower SLP, i.e., a relatively strong Aleutian low. The periods with lower SLP tend to be relatively warm, and followed by less sea ice, as shown in Fig. 6. The Aleutian low tends to be accompanied by a mild air mass of maritime origin, and unless it is displaced well to the east of its typical position, results in relatively warm conditions for the Bering Sea

(Rodionov et al., 2007). Conversely, periods of higher SLP are often accompanied by colder air masses of continental or Arctic origin, as reflected in the composite sea-ice distributions in Fig. 6. There are generally more subtle differences in the composite SLP distributions from top to bottom in the grid of the patterns of Fig. 7; this ordering is more reflective of the sea-ice coverage, which again is weighted more heavily in the construction of the SOM patterns. On the other hand, the overall result is that the SLP distributions with less ice (the bottom row) imply winds more from the southeast through the east, while the SLP distributions with greater ice (the top row) imply winds from the northeast.

As noted above, pattern 6 is somewhat unusual in terms of its more north-south gradient in sea-ice concentration in contrast to the more typical northeast-southwest gradient. The composite SLP map for this group (Fig. 7) implies relatively strong winds from the east. This results in greater poleward Ekman transports near the ice edge, and apparently inhibits the southward extent of ice in the eastern portion of the domain of interest. Pattern 6 also includes a SLP distribution indicative of slightly stronger winds from the northeast, which would serve to promote a tendency for more sea-ice growth in the western portion of the domain than during the other periods.

3.2.2 Timeline of variability

The patterns of ice cover (and SLP) were mapped onto a timeline (Fig. 8). Two temporal patterns immediately arise. First, as expected, the concentrations of ice increase from December through January (i.e., the colors become darker). Second, there appears to be multi-year patterns of ice. For instance, 1988/1989–1994/1995 and 2005/2006–

2013/2014 have extensive ice in January. In contrast, 2014/2015–2016/2017 and 2000/2001–2004/2005 (except 2001/2002) had low concentrations of ice through January. Interestingly, the patterns since 2000 appear to coincide with the warm/cold (low ice extent/extensive ice extent) years in the southern Bering Sea (Stabeno et al., 2012b, 2017). These stanzas of warm (2001–2005, 2014–2016) and cold (2007–2013) have dominated the ecosystem of the southern Bering Sea for almost two decades (Stabeno et al., 2012a; 2017). Since 2000, ice patterns in March and April on the southern Bering Sea shelf appear to be related to ice patterns in the preceding fall and winter on the northern Bering Sea shelf. Before 2000, ice patterns on the southern Bering Sea showed strong year-to-year variability, which was not the case in the northern Bering Sea.

As mentioned previously, pattern 6 had a strong north-south gradient and a relatively weak east-west gradient. This pattern usually dominated for multiple 8-day periods in December-January (e.g., 1984/1985, 2000/2001, and 2015/2016). In addition, during each of these three periods the ice appeared relatively late. In the southern Bering, two out of three of these periods (2001 and 2016) were low ice years with warm ocean conditions, while 1985 (which was before the shift away from high year-to-year variability in the south) had moderate ice in March and April (Stabeno et al., 2012b).

3.2.3 Ice keel depth

Timing and duration are two indicators of variability in sea ice. Another is the draft or keel depth of the ice. Such measurements in the Bering Sea are uncommon, and most are isolated reports of large pieces of ice or from a limited number of ice cores (e.g., Sullivan et al., 2014). In fall 2015, a mooring was deployed to measure ice-keel depth throughout the fall and winter at M8. During the deployment, ice draft data were collected for about four months, beginning in mid-January (Fig. 9). While the daily mean keel depths were relatively small (<1 m), the daily maximum keel depths were substantial. On three different days, the keel depth exceeded 15 m. The deepest keel was on 13 March, exceeding 20 m.

The ice in 2015/2016 (Fig. 8) was largely confined to the northern Bering Sea through January, with a north-south gradient. Ice extended farther south as winter progressed, finally reaching ~57.8°N in early March, and then quickly retreated to north of 62°N by early May (Stabeno et al., 2017). Even though not an extensive ice year in the southern Bering Sea, there were still large (thick) floes of ice present on the northern shelf. Such deep keels present a danger to moorings if the surface float is within 20 m of the surface, thus making measurements in the near-surface waters difficult during winter.

3.3 Temperature, salinity and nutrients at mooring M8

3.3.1 Water column temperature

Temperature, salinity, currents, and chlorophyll fluorescence have been measured at M8 almost continuously since summer 2005. Except for the summer of three years (2005, 2008, and 2009) when short-term moorings with shallower instrumentation were deployed, the upper instrument was at ~20 m. While this design was prudent to avoid possible damage or loss of the mooring due to sea ice, it limits the measurements in the upper part of the water column. Fortunately, the water column typically mixed to below 20 m by late August and remained mixed into late spring (Fig. 10a). So, for late summer through mid-spring the upper water column temperature could be extrapolated to the surface. To examine upper layer temperatures during the rest of the year other sources of data must be found. Two in situ sources of data are available. First, as already mentioned, during three summers data were collected from short-term moorings which sampled the upper water column. Second, temperature profiles were measured on more than 30 hydrographic casts that were conducted in the near vicinity of the mooring during the ice-free months. These casts, also, provide estimates of the mixed layer depth. Temperature in the upper 20 m was linearly interpolated in time when water column sampling (either through moorings or CTDs) occurred within 5 days of each other. The gaps in data in the upper 20 m are evident in Fig. 10b, but reliable daily temperatures exist from September into May throughout the water column and at depths below 20 m during the entire year.

One way to expand the coverage of temperature in the upper water column would be to use SSTs from model output. Daily SST from a variety of models were compared to the measured near surface temperatures at M8. The model output that was best correlated to observations was NASA JPL's MUR analysis. The annual cycle of monthly MUR SST and monthly near-surface temperature from M8 compare well (Fig. 11a). The monthly SSTs ranged from a maximum of >9 °C in August to a minimum of approximately -1.7 °C in February through April. During May–August the MUR SST is slightly warmer than that measured at M8. The likely cause of this is that the summer measurements at M8 were dominated by three years with more extensive ice and thus colder temperatures. The daily SST MUR anomalies were calculated relative to the mean daily MUR SSTs (2002–2017) and the daily near-surface temperature anomalies were calculated relative to the daily mean SST measured at M8 (2005–2017). The daily SST anomalies from MUR were correlated ($p<0.01$) with the anomalies at M8, however, deviations could be as large as ±5°C (Fig. 11b), while variability of the monthly average SST anomalies (blue dots in Fig. 11b) was much reduced. So, while monthly mean MUR SST provides a reliable estimate of temperature, the daily MUR SST would not be helpful in filling the missing temperatures in the upper 20 m in Fig. 10b.

Summer mean SST anomalies (MUR) are negatively correlated (R^2=0.5; $p<0.01$) with date of ice retreat (2002–2017)—that is, early ice retreat was associated with warmer summer (June–September) temperatures (not shown). While temperature anomalies from February through April were near zero, the anomalies in June through September tended to vary by year—some years warmer (e.g., 2002–2004, 2014, 2016) and some colder (2009, 2011, 2012) (Fig. 11c). The warmer-than-average years were typically found in bands (or groups) with less ice in December and January, while cooler than average years were in bands of years of more extensive ice in December and January (Fig. 8).

3.3.2 Mean ocean temperature and anomalies

The 13 years of ice and temperature data shown in Figs. 10a and 10b were averaged to create an annual signal (Fig. 12). Sea ice is present and the water column remains cold from January until early June; the near surface begins to warm in June when sea ice disappears. In September, the water column begins to mix and is typically well mixed by mid to late November. With the arrival of ice, the water column continues to cool. By late December the water column reaches its near minimum temperature of –1.7 °C.

Temperature anomalies at M8 (Fig. 10c) were derived relative to the annual temperature signal (Fig. 12b). The entire water column was warmer than average in 2005, 2014/2015 and especially in late 2016. The greatest anomalies in the water-column temperature structure occurred at the interface between the wind-mixed layer and deeper water (~20–30 m), and during warm periods in fall 2014 through early 2017 (Fig. 10c). Both the cool and warm anomalies at the bottom of the mixed layer are associated with timing of mixing. For instance, delayed fall storms limit mixing and result in cooler temperatures below the mixed layer (e.g., 2008, 2013). Deeper mixed layers (e.g., 2015) and early storm activity (e.g., 2005) result in warmer temperatures below the mixed layer.

Fall winds serve to mix the water column and hence cause warming near the bottom; the entire column then cools slowly due to the loss of heat to the atmosphere. The arrival and melting of sea ice cools and freshens the surface. This cold water is mixed vertically on time scale of a week (Sullivan et al., 2014). The rapid cooling of the bottom following the arrival of sea ice is evident in 2005, 2015, and 2017 (Fig. 13). When ice is delayed, the warm bottom temperatures can persist into January (e.g., 2015 and 2017).

3.3.3 Salinity

The temporal variability of salinity is shown at two depths: 30 m and 55 m (Fig. 14). The pattern at 30 m has the highest salinity in April decreasing through September as the surface freshwater lens mixes vertically. In early October, the water column continues to mix, entraining more saline bottom water and thus increasing the salinity at 30 m. In December, the water column has mixed nearly to the bottom, and salinity at 30 and 55 m are largely in agreement. As the winter progresses the water column becomes more saline. From April into November the salinity near the bottom (55 m), in contrast to the salinity at 30 m, freshens only slightly.

Two sources of water in the vicinity of M8 are flow along the 100-m isobath which originates on the southern shelf and the onshelf flow of slope water through Zhemchug Canyon (Fig. 1; Stabeno et al., 2017). At M8, the daily mean currents at 55 m are highly variable, but the annual mean flow is weak toward the north-northwest ($u = -0.16 \pm 0.13$ cm s^{-1} [±SEM], $v = 0.27 \pm 0.16$ cm s^{-1}). During December–March the mean currents are slightly stronger and toward the northwest ($u=-0.32 \pm 0.24$ cm s^{-1}, $v=0.39 \pm 0.30$ cm s^{-1}). (The data used in the velocity calculations were collected during September 2005–September 2009, September 2010–September 2012, and September 2013–September 2017.) The slope and outer shelf (that part of the shelf where water depth ranges from 100 to 180 m) has salinities >32, and are likely one source of the more saline water that replenishes the region around M8 in December through March. An additional sporadic source of more saline water is brine rejection during ice formation, especially in the polynya south of St. Lawrence Island.

An examination of the monthly mean salinity anomalies at M8 reveals a multi-year pattern of variability (Fig. 15). From 2005 to 2008, salinity at M8 was often >32.4, but from 2008 to 2014 there was a decrease in salinity by almost 1; this was especially evident in the near-bottom water. This period largely coincides with the group years of colder SST and more extensive sea ice in the spring. Similar freshening occurred to the south at moorings M4 and M5 (see Fig. 1 for locations). For instance, at M4, the water column freshened by ~1 from 2006 (reported as an average ice year in the south in

Stabeno et al., 2012b) to 2007 (an extensive ice year) and these lower salinities persist until 2014, when the southern shelf shifted to a series of years of less ice. Similarly, salinity decreased at M5 during this period (Stabeno et al., 2012a). A similar decrease in salinity was also observed at Bering Strait (Woodgate, 2018). With the return of low ice extents in 2014 (Stabeno et al., 2017), salinities increased at M4. This increase occurred more than a year earlier than was observed at M8, which is consistent with the southern Bering Sea being a possible source of the more saline water. It takes approximately one year for water to travel from the southern shelf to the vicinity of St. Lawrence Island (Stabeno et al., 2016).

3.3.4 Nutrients

To assess the seasonal variability of nutrients near the M8 mooring, data within a 1° latitude × 2° longitude box (61.8–62.8 °N, 174–176°W) around the mooring site were examined. The data set includes 696 measurements of nitrate, nitrite, silicic acid, phosphate, and ammonium at 166 stations collected during 22 cruises between 2005 and 2017 (Table S1). The majority of cruises (15) occurred during years with more extensive ice (2007–2012; Fig. 8).

In the bottom layer (45–80 m) near the M8 mooring site, there is considerable variability in the concentrations of nitrate and silicic acid (Figs. 16a and 16b). Much of this variability resulted from the vertical nutrient gradients in the bottom layer. For example, in spring 2007, the gradient between samples collected in the bottom layer averaged 2.8 µM nitrate and 5.8 µM silicic acid. Vertical gradients were also observed in salinity suggesting that nutrient variability was the result of physical rather than biological forcing. Even with this variability, the bottom waters displayed a small, but significant ($p < 0.001$), seasonal signal with the highest nitrate, dissolved inorganic nitrogen (DIN) and silicic acid concentrations observed during ice retreat (April and May), and lower concentrations in fall (September–October) and late winter (March) (Fig. 16, Table 1). This pattern is consistent with nutrient replenishment beginning in fall and continuing until ice retreat in spring, although inter-annual variability between observations in March and in April-May cannot be discounted. On the northern middle shelf, a relatively thick pycnocline overlaps the euphotic zone, and this frequently results in a subsurface chlorophyll maxima within the pycnocline (Stabeno et al., 2012a). The decrease in the deep nutrient pool during summer may in part be caused by this sub-pycnocline phytoplankton production.

In the upper water column (0–15 m; Figs. 17a and 17b), the highest concentrations of nitrate and silicic acid were observed during the period of ice retreat (April–May), with concentrations of 12.7 ± 0.3 µM (82) and 35.4 ± 0.6 µM (82), respectively (mean ± SEM [number of samples]). These nutrient levels were significantly lower ($p < 0.0001$) than simultaneous measurements in April–May made in deeper water (Table 1; Figs. 16a and 16b), a result consistent with the onset of primary productivity from ice-associated algae and/or from phytoplankton. Assuming that seasonal patterns in nitrate were similar in all years, by early June nitrate is nearly depleted in the upper water column (Fig. 17a). (Data below 15 m are not shown, but mean nitrate in June was 0.5 and 3.7 µM at 20 m and 30 m, respectively). Integrating seasonal (April to June) changes in nitrate and ammonium over the upper 30 m, and assuming a molar uptake ratio of 106C:16N (Redfield, 1958), net community production was 31 g C m^{-2}, a value similar to previous findings of 33 g C m^{-2} over the entire northern middle shelf (Mordy et al., 2012). This drawdown occurred in ~ 30 days, equivalent to a rate of ~ 1 g C m^{-2} d^{-1}, a value similar to measurements of net primary production in the region (0.05–2.53 g C m^{-2} d^{-1}; Lomas et al., 2012). The concomitant loss of silicic acid (Fig. 17b) was indicative of diatom production. While the Si:N drawdown ratio in June (2.2) exceeded the traditional Si:N ratio for vegetative diatom production (~1) (Brzezinski, 1985), higher ratios have been observed under nitrogen limiting conditions (Kudo, 2003; Sugie et al., 2010).

Ammonium is formed through the remineralization of organic matter, and is subsequently oxidized into nitrate through nitrification (Lomas and Lipschultz, 2006). Ammonium concentrations in the bottom layer were relatively constant from March to June, averaging 1.1 ± 0.05 μM (112), but increased significantly to 2.9 ± 0.1 μM (237, $p < 0.0001$) during the ice-free months (Fig. 16c). It is hypothesized that through the winter, remineralization and nitrification are roughly in balance, such that ammonium concentrations remain relatively stable while nitrate concentrations are replenished. Concomitant with ice retreat and increasing primary and secondary production in spring, organic matter (including ice-associated algae) is exported to the bottom layer and benthos, and through the summer, ammonification exceeds nitrification resulting in a build-up of ammonium. This simplified supposition neglects other important physical processes (e.g. advection/diffusion) and biological processes (e.g. phytoplankton assimilation below the pycnocline, Stabeno et al., 2012a) that influence ammonium concentrations.

Between June and October, ammonium accumulated within the bottom (45–80 m) layer at a rate of 0.8 ± 0.1 mmol m^{-2} d^{-1} ($p < 0.0001$). Stable isotope studies have found that sedimentary efflux serves as the primary source of ammonium in overlying waters (Granger et al., 2011; Morales et al., 2014), and the observed ammonium accumulation rate in Fig. 16c is approximately the same as some direct measurements of the sedimentary ammonium efflux (Lomstein et al., 1989; Henriksen et al., 1993). Other direct measurements have low or near zero efflux (see Table 5 in Horak et al., 2013). These differences may be related to spatial and temporal (seasonal and interannual) variability inherent in instantaneous measurements compared to isotopic measurements that integrate over space and time.

In the upper water, ammonium concentrations, unlike nitrate, decline in spring from 1.3 ± 0.1 μM (17) in March to 0.7 ± 0.1 μM (82) in April-May ($p < 0.0001$) (Figs. 17a and 17c). This finding is consistent with preferential ammonium uptake in ice-covered waters in spring (Morales et al., 2014). While ammonium was measurable in surface waters through the summer, the balance between physical (e.g., advection/diffusion) and biological (e.g., phytoplankton uptake, nitrification, ammonification) processes remains unknown.

The temporal variability of nutrients near the M8 mooring was determined by subsampling for stations between July and mid-October (to eliminate seasonality), and selecting for the deepest sample per cast within the 60–80 m depth range (samples were generally within 5 m of the bottom). The number of samples per cruise varied widely, so the yearly mean was determined from the mean value for each cruise. No significant trend was observed for silicic acid, but between 2005 and 2016, there was a significant reduction in the bottom water concentrations of DIN ($p = 0.0007$) and phosphate ($p = 0.02$) (Figs. 18a and 18b). Associated with this decrease in nutrient content was freshening of ~1 psu (Fig. 15). The freshening indicates that the decadal reduction in nutrient content was likely mediated by physical (advection along the 100-m isobath) rather than biological processes. In 2017, phosphate and DIN concentrations increased concomitant with an increase in salinities at 30 m (Fig. 15; salinity at 55 m was unavailable in 2017).

3.3.5 Zooplankton

The abundance of *Calanus* spp. showed multiple patterns over the past decade. During years of early ice retreat (2005, 2014–2015), early stages of *Calanus* spp. were largely absent from the plankton (Fig. 19). The opposite was observed during years of late ice retreat (2008–2010) where considerable numbers of early stage copepodites were observed. These observations agree with what has been reported for *Calanus* spp. (cited as *C. marshallae* in Napp et al. (2002)) on the southeastern Bering Sea shelf across warm and cold periods (Napp et al., 2002; Campbell et al., 2016; Kimmel et al., 2018). The initiation of reproduction in association with ice algae has been demonstrated in the northern Bering Sea (Durbin and Casas, 2014) and Hudson Bay, Canada (Runge et al., 1991). By analogy, *Calanus* spp. initiate reproduction after emergence from diapause by consuming ice-associated algae, as has been observed for *C. glacialis* in Rijpfjorden, Svalbard as well (Søreide et al., 2010).

In *Calanus* spp., the timing of the ice retreat determines when reproduction begins, and subsequent warming determines the development rate of the offspring. These combined effects result in the variability observed among the early (C1-C4) life-history stages in response to ice retreat and temperature. For example, a high number of adults were present in the very cold year 2009 (Fig. 19), suggesting that the late ice retreat in this year resulted in the presence of some reproducing adults much later in the year than is normally observed. It is also interesting to note that the abundance of *Calanus* spp. C5 copepodites appeared largely unchanged over time. For *Calanus* spp., diapause is thought to occur in the C5 stage, but has been reported to occur in the C4 or C6 stage as well, depending on location (Baumgartner and Tarrant, 2017), though direct reports from the Pacific Ocean basin are limited. Temperature affects this pattern, i.e., in cold years *Calanus* spp. may not enter diapause at the C5 stage, whereas in warm years, all copepodites are likely to have made it to the C5 stage and enter into diapause early. Therefore, it was not surprising that C5 abundance did not change because during a cold year, more C5 may be in the water column prior to diapause, whereas in a warm year, more copepodites have made it to the C5 stage, but many C5 may have already exited the water column and entered diapause. This differs from observations in the southeastern Bering Sea (Napp et al., 2002; Kimmel et al., 2018) where *Calanus* spp. C5 were in low abundance, or absent, from the plankton in the fall. This observation suggests that the lower temperatures near M8 result in more *Calanus* spp. C5 being present in late-summer/early-fall as compared to the southeastern shelf where *Calanus* spp. C5 would have entered diapause. Despite substantial changes in the timing of ice retreat, the *Calanus* spp. population appears to obtain similar pre-diapause abundances from year-to-year.

4. Summary and conclusions

The northern Bering Sea is part of the Pacific Arctic marine ecosystem, and as such is predicted to be sensitive to climate change (IPCC Climate Change, 2007). Prior to 2014, however, there had been no trend in the time of ice arrival, retreat nor duration in the vicinity of M8. On average (1980–2017), ice arrived at M8 in late December and departed in mid-May, thus areal ice cover (>20%) persisted for an average of ~140 days. Since 2014, the arrival date of ice has been later and the retreat date earlier, reaching an extreme in 2017/2018 with ice being present at ~18% areal cover for only one day in mid-March. On average, the changes observed during the last four years fall within changes predicted to occur in the next 30 years—ice will retreat 10–20 days earlier, and arrive 10–20 days later, resulting in a decrease of 20–30 days in the annual duration of ice (Wang et al., 2018).

Formation, advance, and retreat of sea ice are primarily a result of atmospheric forcing. Less ice is associated with wind anomalies out of the east to southeast, while more extensive ice is associated with stronger winds from the northeast (Figs. 6 and 7). Periods with a strong Aleutian low, with its mild air mass, are associated with less sea ice. Conversely, periods of higher SLP with cold air of continental and/or Arctic origin support more extensive sea ice. Historically the southern Chukchi freezes before the northern Bering Sea.   The southern Chukchi freezes ~30 days later than it did in in the early 1980s (Fig. 4), which will may begin to impact the timing of ice arrival in the vicinity of M8.

One surprising result from this research was the multi-year patterns of variability in sea-ice cover during December and January of each ice year. The common pattern of extensive ice in January was interrupted by short periods (2–5 years) of low areal ice concentrations in the vicinity of M8. Since 2000, these low ice years in the north often appeared related to low ice periods in the southern Bering Sea. The connection was likely a combination of two factors: first, persistence during the winter of atmospheric patterns that did not promote sea-ice formation and advection of existing sea ice southward; and second, the delay of sea-ice formation in the north that decreased the time (maximum ice extent usually occurs in March) available for ice to be advected southward. Note, that sea ice in the southern Bering Sea is largely advected (Sullivan et al., 2014), and the main ice formation areas in the Bering Sea are the polynyas at St. Lawrence and St. Matthew Islands, and along the Alaskan and Siberian coasts. While there may be a delay in ice formation, it must be noted that ice can move very rapidly over the Bering Sea shelf—in 2007/2008 sea ice was advected ~1000 km, transforming the eastern shelf from a region of little ice to largely ice covered, in less than 30 days (Stabeno et al., 2012a).

The question arises whether delayed arrival of sea ice in the northern Bering Sea is going to be the “new normal”. Historically, sea ice arrived in the northern Bering Sea in December and had at least three months to grow in extent before the onset of greater insolation and the typically warmer weather in April. If warm intervals such as occurred in February 2018 also become more frequent, then delayed date of ice arrival will result in lesser maximum ice extents for the Bering Sea, with a host of consequences for the regional marine ecosystem.

Sea ice directly affects the ecosystem. Early ice retreat in spring was correlated with warmer SST during summer. Late ice arrival in the fall/winter was related to warmer bottom temperatures. Increases in water column temperatures were particularly evident in 2015–2017. The timing of ice retreat on the Bering Sea shelf influences the timing of primary production in the spring (Sigler et al., 2014). The timing of ice retreat and warmer conditions also impact timing of reproduction and development rate of *Calanus* spp. For instance, during years when ice retreated earlier, there were fewer early life history stages of *Calanus* spp. (and vice versa). Warmer bottom temperatures, which reached >4°C for short periods in 2016, can also influence benthic production (e.g., increasing metabolic rate during fall).

The northern Bering Sea is identified as an inflow shelf (Carmack and Wassmann, 2006) and is the source waters for the Chukchi Sea. Changes in ocean temperature, nutrient concentrations and zooplankton populations in the Bering Sea will likely impact the Chukchi Sea ecosystem. The reduction in sea ice will also impact transportation, marine mammal habitat, coastal erosion, and the inhabitants of coastal communities who depend on ice for access to resources (hunting) and also for protection from storm driven waves along the coast.

Acknowledgements

This research is contribution 4782 from NOAA/Pacific Marine Environmental Laboratory, 0906 to NOAA’s Ecosystems Fisheries Oceanography Coordinated Investigations. This publication is partially funded by Joint Institute for the Study of the Atmosphere and Ocean, University of Washington, contribution 2018-0151. The research was supported by grants from the North Pacific Research Board (Grants: #517, 602, 701, 1302, and B52) and by NOAA's Ecosystems Fisheries Oceanography Coordinated Investigations. This publication is primarily funded by NOAA and partially funded by the Joint Institute for the Study of the Atmosphere and Ocean (JISAO) under NOAA Cooperative Agreement NA10OAR4320148.

Table 1. Concentrations of nutrients [mean ± standard error of the mean (N)] in deep water (45–80 m) near the M8 mooring (61.7°–62.7°N, 174°–176°W). P-values < 0.0001 indicate extremely statistically significant differences (t-test) between concentrations in spring and those in fall and winter.

Nutrient	All Data (Mar - Oct) (µM)	Early Ice Retreat (Apr - May) (µM)	Fall (Sep - Oct) (µM)	P-value	Winter (March) (µM)	P-value
Nitrate	12.7 ± 0.2 (349)	15.1 ± 0.4 (83)	11.7 ± 0.2 (139)	<0.0001	10.4 ± 0.6 (15)	<0.0001
DIN	15.1 ± 0.2 (349)	16.3 ± 0.4 (83)	15.2 ± 0.2 (139)	<0.0001	12 ± 0.7 (15)	<0.0001
Silicic Acid	34.8 ± 0.5 (349)	41.1 ± 0.9 (83)	33.5 ± 0.7 (139)	<0.0001	30.3 ± 1.9 (15)	<0.0001

References

Baumgartner, M.F., Tarrant, A.M., 2017. The physiology and ecology of diapause in marine copepods. Ann. Rev. Mar. Sci. 9, 387–411.

Brzezinski, M.A., 1985. The Si: C: N ratio of marine diatoms: interspecific variability and the effect of some environmental variables. J. Phycol. 21(3), 347–357.

Campbell, R.G., Ashjian, C.J., Sherr, E.B., Sherr, B.F., Lomas, M.W., Ross, C., Alatalo, P., Gelfman, C., Van Keuren, D., 2016. Mesozooplankton grazing during spring sea-ice conditions in the eastern Bering Sea. Deep-Sea Res. Part II 134, 157–172.

Carmack, E., Wassmann, P., 2006. Food webs and physical–biological coupling on pan-Arctic shelves: unifying concepts and comprehensive perspectives. Prog. Oceanogr. 71, 446–477.

Cassano, J.J., Cassano, E.N., Seefeldt, M.W., Gutowski, Jr. W.J., Gilisan, J.M., 2016. Synoptic conditions during wintertime temperature extremes in Alaska. J. Geophys. Res. Atmos, 121, 3241–3262. https://doi.org/10.1002/2015JD024404

Chin, M.T, Vazquez-Cuervo, J., Armstrong, E.M., 2017. A multi-scale high-resolution analysis of global sea surface temperature, Remote Sens. Environ. 200, 154–169. https://doi.org/10.1016/j.rse.2017.07.029.

Comiso, J.C., 2017. Bootstrap Sea Ice Concentrations from Nimbus-7 SMMR and DMSP SSM/I-SSMIS, Version 3. NASA National Snow and Ice Data Center Distributed Active Archive Center, Boulder, CO. https://doi.org/10.5067/7Q8HCCWS4I0R [Accessed 2017].

Danielson, S.L., Weingartner, T.J., Aagaard, K., Zhang, J., Woodgate, R.A., 2012. Circulation on the central Bering Sea shelf, July 2008–July 2010. J. Geophys. Res. 117, C10003. https://doi.org/10.1029/2012JC008303.

Dore, J.E., Houlihan, T., Hebel, D.V., Tien, G., Tupas, L., Karl, D.M., 1996. Freezing as a method of sample preservation for the analysis of dissolved inorganic nutrients in seawater. Mar. Chem. 53(3), 173–185.

Durbin, E.G., Casas, M.C., 2014. Early reproduction by *Calanus glacialis* in the Northern Bering Sea: The role of ice algae as revealed by molecular analysis. J. Plankton Res. 36, 523–541.

Eisner, L.B., Gann, J.C., Ladd, C., Cieciel, K.D., Mordy, C.W., 2016. Late summer/early fall phytoplankton biomass (chlorophyll a) in the eastern Bering Sea: Spatial and temporal variations and factors affecting chlorophyll-a concentrations. Deep-Sea Res. Part II 134, 100–114. https://doi.org/10.1016/j.dsr2.2015.07.012.

Gordon, L.I., Jennings Jr., J. C., Ross, A.A., Krest, J.M., 1993. A suggested protocol for continuous flow automated analysis of seawater nutrients (phosphate, nitrate, nitrite and silicic acid) in the WOCE Hydrographic Program and the Joint Global Ocean Fluxes Study, Methods Manual WHPO 91–1, WHP Operations and Methods, WOCE Hydrographic Program Office, La Jolla, CA.

Granger, J., Prokopenko, M.G., Sigman, D.M., Mordy, C.W., Morse, Z.M., Morales, L.V., Sambrotto, R.N., Plessen, B., 2011. Coupled nitrification-denitrification in sediment of the eastern Bering Sea shelf leads to ^{15}N enrichment of fixed N in shelf waters. J. Geophys. Res. Oceans 116, C11006. https://doi.org/10.1029/2010JC006751.

Grebmeier, J.M., 2012. Shifting patterns of life in the Pacific arctic and sub-arctic seas. Ann. Rev. Mar. Sci. 4, 63–78. https://doi.org/10.1146/annurev-marine-120710-100926.

Grebmeier, J.M., Overland, J.E., Moore, S.E., Farley, E.V., Carmack, E.C., Cooper, L.W., Frey, K.E., Helle, J.H., McLaughlin, F.A., McNutt, S.L., 2006. A major ecosystem shift in the northern Bering Sea. Science 311(5766), 1461–1464. https://doi.org/10.1126/science.1121365.

Henriksen, K., Blackburn, T.H., Lomstein, B.A., McRoy, C.P., 1993. Rates of nitrification, distribution of nitrifying bacteria and inorganic N fluxes in northern Bering-Chukchi shelf sediments. Cont. Shelf Res. 13(5–6), 629–651.

Horak, R.E., Whitney, H., Shull, D.H., Mordy, C.W., Devol, A.H., 2013. The role of sediments on the Bering Sea shelf N cycle: Insights from measurements of benthic denitrification and benthic DIN fluxes. Deep-Sea Res. Part II 94, 95–105.

Hunt, Jr., G.L., Coyle, K.O., Eisner, L., Farley, E.V., Heintz, R., Mueter, F., Napp, J.M., Overland, J.E., Ressler, P.H., Salo, S., Stabeno, P.J., 2011. Climate Impacts on eastern Bering Sea foodwebs: A synthesis of new data and an assessment of the Oscillating Control Hypothesis. ICES J. Mar. Sci. 68(6), 1230–1243. https://doi.org/10.1093/icesjms/fsr036.

IPCC Climate Change, 2007. The Physical Science Basis. In: Solomon, S., Qin, D., Manning, M., Chen, Z., Marquis, M., Averyt, K.B., Tignor, M., Miller, H.L. (Eds.), Contribution of Working Group I to the Fourth Assessment Report of the Intergovernmental Panel on Climate Change. Cambridge University Press, Cambridge and New York, NY.

Kalnay, E., Kanamitsu, M., Kistler, R., Collins, W., Deaven, D., Gandin, L., Iredell, M., Saha, S., White, G., Woollen, J., Zhu, Y., Leetmaa, A., Reynolds, R., Chelliah, M., Ebisuzaki, W., Higgins, W., Janowiak, J., Mo, K.C., Ropelewski, C., Wang, J., Jenne, R., Joseph, D., 1996. The NCEP/NCAR 40-Year Reanalysis Project. Bull. Am. Meteorol. Soc. 77, 437–471. https://doi.org/10.1175/1520-0477(1996)077<0437:TNYRP>2.0.CO;2.

Kanamitsu, M., Ebisuzaki, W., Woollen, J., Yang, S.-K., Hnilo, J.J., Fiorino, M., Potter, G.L., 2002. NCEP-DOE AMIP-II Reanalysis (R-2). Bull. Am. Meteorol. Soc. 83, 1631–1643.

Kimmel, D.G., Eisner, L.B., Wilson, M.T., Duffy-Anderson, J.T., 2018. Copepod dynamics across warm and cold periods in the eastern Bering Sea: Implication for walleye pollock (*Gadus chalcogrammus*) and the Oscillating Control Hypothesis. Fish. Oceanogr. 27(2), 143–158.

Kinder, T.H., Chapman, D.C., Whitehead, Jr., J.A., 1986. Westward intensification of the mean circulation on the Bering Sea shelf. J. Phys. Oceanogr. 16, 1217–1229.

Kudo, I., 2003. Change in the uptake and cellular Si: N ratio in diatoms responding to the ambient Si: N ratio and growth phase. Mar. Biol. 143(1), 39–46.

Liu, H., Hopcroft R.R., 2007. A comparison of seasonal growth and development of the copepods *Calanus marshallae* and *C. pacificus* in the northern Gulf of Alaska. J. Plankton Res. 29, 569–581.

Liu, Y., Weisberg, R.H., 2011. A review of Self-Organizing Map applications in meteorology and oceanography. In: Mwasiagi, J.I. (Ed.), Self-Organizing Maps–Applications and Novel Algorithm Design. InTech, Rijeka, Croatia, pp.253–272. https://dx.doi.org/10.5772/13146.

Lomas, M.W., Lipschultz, F., 2006. Forming the primary nitrite maximum: Nitrifiers or phytoplankton? Limnol. Oceanogr. 51(5), 2453–2467.

Lomas, M.W., Moran, S.B., Casey, J.R., Bell, D.W., Tiahlo, M., Whitefield, J., Kelly, R.P., Mathis, J.T., Cokelet, E.D., 2012. Spatial and seasonal variability of primary production on the Eastern Bering Sea shelf. Deep-Sea Res. Part II 65, 126–140.

Lomstein, B.A., Blackburn, T.H., Henriksen, K., 1989. Aspects of nitrogen and carbon cycling in the northern Bering Shelf sediment. I. The significance of urea turnover in the mineralization of NH_4^+. Mar. Ecol. Prog. Ser. 57(3), 237–247.

Macdonald, R.W., McLaughlin, F.A., Wong, C.S., 1986. The storage of reactive silicate samples by freezing. Limnol. Oceanogr. 31(5), 1139–1142.

Mantoura, R.F.C., Woodward, E.M.S., 1983. Optimization of the indophenol blue method for the automated determination of ammonia in estuarine waters, Estuar. Coast. Shelf Sci. 17(2), 219–224.

Maslanik, J., Stroeve, J., 1999, updated daily. Near-Real-Time DMSP SSMIS Daily Polar Gridded Sea Ice Concentrations, Version 1. NASA National Snow and Ice Data Center Distributed Active Archive Center, Boulder, CO. https://doi.org/10.5067/U8C09DWVX9LM. [Accessed 2018].

Morales, L.V., Granger, J., Chang, B.X., Prokopenko, M.G., Plessen, B., Gradinger, R., Sigman, D.M., 2014. Elevated $^{15}N/^{14}N$ in particulate organic matter, zooplankton, and diatom frustule-bound nitrogen in the ice-covered water column of the Bering Sea eastern shelf. Deep-Sea Res. Part II 109, 100–111.

Mordy, C.W., Cokelet, E.D., Ladd, C., Menzia, F.A., Proctor, P., Stabeno, P.J., Wisegarver, E., 2012. Net community production on the middle shelf of the eastern Bering Sea. Deep-Sea Res. Part II 65, 110–125.

Napp, J.M., Baier, C.T., Brodeur, R.D., Coyle, K.O., Shiga, N., Mier, K., 2002. Interannual and decadal variability in zooplankton communities of the southeast Bering Sea shelf. Deep-Sea Res. Part II 49, 5991–6008.

Redfield, A.C., 1958.The biological control of chemical factors in the environment. Am. Sci. 46, 205–221.

Runge, J.A., Therriault, J.-C., Legendre, L., Ingram, R.G., Demers, S., 1991. Coupling between ice microalgal productivity and the pelagic, metazoan food web in southeastern Hudson Bay: A synthesis of results. Polar Res. 10, 325–338.

Rodionov, S.N., Bond, N.A., Overland, J.E., 2007. The Aleutian Low, storm tracks, and winter climate variability in the Bering Sea, Deep-Sea Res. Part II 54(23-26), 2560–2577.

Serreze, M.C., Stroeve, J., Barrett, A.P., Boisvert, L.N., 2016. Summer atmospheric circulation anomalies over the Arctic Ocean and their influences on September sea ice extent: A cautionary tale. J. Geophys. Res. Atmos. 121(19), 11,463–11,485. https://doi.org/10.1002/2016JD025161.

Sigler, M.F., Stabeno, P.J., Eisner, L.B., Napp, J.M., Mueter, F.J., 2014. Spring and fall phytoplankton blooms in a productive subarctic ecosystem the eastern Bering Sea, during 1995-2011. Deep-Sea Res. Part II 109, 71–83. https://doi.org/10.1016/j.dsr2.2013.12.007.

Søreide, J.E., Leu, E.V.A., Berge, J., Graeve, M., Falk-Petersen, S., 2010. Timing of blooms, algal food quality and *Calanus glacialis* reproduction and growth in a changing Arctic. Glob. Change Biol. 16, 3154–3163.

Stabeno, P.J., Danielson, S., Kachel, D., Kachel, N.B., Mordy, C.W., 2016. Currents and transport on the eastern Bering Sea shelf: An integration of over 20 years of data. Deep-Sea Res. Part II 134, 13–29. https://doi.org/10.1016/j.dsr2.2016.05.010.

Stabeno, P.J., Duffy-Anderson, J.T., Eisner, L.B., Farley, E.V., Heintz, R.A., Mordy, C.W., 2017. Return of warm conditions in the southeastern Bering Sea: Physics to fluorescence. PLoS One 12(9), e0185464. https://doi.org/10.1371/journal.pone.0185464.

Stabeno, P.J., Farley, E., Kachel, N., Moore, S., Mordy, C., Napp, J.M., Overland, J.E., Pinchuk, A.I., Sigler, M.F., 2012a. A comparison of the physics of the northern and southern shelves of the eastern Bering Sea and some implications for the ecosystem. Deep-Sea Res. Part II 65–70, 14–30. https://doi.org/10.1016/j.dsr2.2012.02.019.

Stabeno, P.J., Kachel, N.B., Moore, S.E., Napp, J.M., Sigler, M., Yamaguchi, A., Zerbini, A.N., 2012b. Comparison of warm and cold years on the southeastern Bering Sea shelf and some implications for the ecosystem. Deep-Sea Res. Part II 65–70, 31–45. https://doi:10.1016/j.dsr2.2012.02.020.

Stabeno, P.J., Napp, J., Mordy, C., Whitledge, T., 2010. Factors influencing physical structure and lower trophic levels of the eastern Bering Sea shelf in 2005: Sea ice, tides and winds. Prog. Oceanogr. 85(3–4), 180–196. https://doi.org/10.1016/j.pocean.2010.02.010.

Sugie, K., Kuma, K., Fujita, S., Ikeda, T., 2010. Increase in Si: N drawdown ratio due to resting spore formation by spring bloom-forming diatoms under Fe-and N-limited conditions in the Oyashio region. J. Exp. Mar. Biol. Ecol. 382(2), 108–116.

Sullivan, M.E., Kachel, N.B., Mordy, C.W., Salo, S.A., Stabeno, P.J., 2014. Sea ice and water column structure on the eastern Bering sea shelf. Deep-Sea Res. Part II 109, 39–56. https://doi.org/10.1016/j.dsr2.2014.05.009.

Wang, M., Overland, J.E., 2009. A sea ice free summer Arctic within 30 years? Geophys. Res. Lett. 36, L07502. https://doi.org/10.1029/2009GL037820.

Wang, M., Yang, Q., Overland, J.E., Stabeno, P.J., 2018. Sea-ice cover timing in the Pacific Arctic: The present and projections to mid-century by selected CMIP5 models. Deep-Sea Res. Part II, SOAR II Special Issue. https://doi.org/10.1016/j.dsr2.2017.11.017.

Wehrens, R., 2015. (Sept 04). Package 'kohonen' [Online]. Available: https://cran.r-project.org/web/packages/kohonen/kohonen.pdf

Wood, K.R., Bond, N.A., Overland, J.E., Salo, S.A., Stabeno, P., Whitefield, J., 2015. A decade of environmental change in the Pacific Arctic region. Prog. Oceanogr. 136, 12–31. https://doi.org/10.1016/j.pocean.2015.05.005.

Wood, K.R., Jayne, S.R., Mordy, C.W., Bond, N., Overland, J.E., Ladd, C., Stabeno, P.J., Ekholm, A.K., Robbins, P.E., Schreck, M.-B., Heim, R., Intrieri, J., 2018. Results of the first Arctic Heat Open Science Experiment. Bull. Am. Meteorol. Soc., 99(3), 513–520. https://doi.org/10.1175/BAMS-D-16-0323.1.

Woodgate, R.A., 2018. Increases in the Pacific inflow to the Arctic from 1990 to 2015, and insights into seasonal trends and driving mechanisms from year-round Bering Strait mooring data. Prog. Oceanogr. 160, 124–154. https://doi.org/10.1016/j.pocean.2017.12.007.

Figure Captions

Figure 1. DBO-1 is indicated approximately by the blue box to the west of St. Lawrence Island. Mooring locations M2, M4, M5, and M8 are indicted. The flow patterns are adapted from Stabeno et al. (2017) and do not include the Alaskan Coastal Current nor the circulation around Pribilof Islands.

Figure 2. The sampling area for sea-ice concentration (black dots) and sea level pressure (red dots). The region in the Chukchi Sea where ice cover was calculated is outlined in purple.

Figure 3. (a) Timing of the arrival (areal ice concentration >20%) of sea ice in the 50 km × 50 km box centered at M8. (b) The day of ice retreat (areal ice concentration is <20%). (c) The number of days between when ice arrives and departs the box around M8. The data points for 2017-2018 are open circles, indicating that these data are an interim product not the final bootstrap data product and that the estimated areal ice coverage is only 18%. In each panel, the dashed line indicates the mean of data set, excluding the 2018 data.

Figure 4. Time series of ice arrival 50 km × 50 km box centered at M8 (>20%) and the timing of 80% ice cover in southern Chukchi. Mean date at M8 of arrival is day 361 (27 December), and mean date for the southern Chukchi is day 332 (27 November). In 2018, sea-ice concentration only reached 18% at M8, which is indicated by the open circle.

Figure 5. Patterns of average (1979–2017) ice cover in 8-day periods from December 1 through February 2.

Figure 6. The 12, 8-day patterns of sea ice derived by SOM. The accompanying SLP patterns are shown in Fig. 7. The patterns are color coded in the lower part of each panel, from white (lowest ice concentration, pattern 3) to black (highest ice concentration, pattern 10) in shades of gray. Pattern 6 has the strongest north-south gradient. These color codes (gray) are used in Fig. 8. The numbers in the upper right-hand corners indicate the number of maps used in calculating that pattern.

Figure 7. The 12, 8-day patterns of SLP calculated from SLPA derived by SOM. The number in the lower right-hand corner indicates the pattern number. The accompanying sea-ice patterns are shown in Fig. 6.

Figure 8. Timeline of SOM patterns. Patterns are indicated by shades of gray (Fig. 6) and by the small number in each box. Note that the darker the color the more ice in the pattern. The yellow indicates pattern 6, with a strong north-south gradient. The warm (red) and cold (blue) years at the southern mooring, M2, are indicated on the right (data from Stabeno et al., 2017). The striped line indicates period of high year-to-year variability. The winter/spring of 2006 and 2017 had average ice cover, which is indicated by white.

Figure 9. Time series of daily maximum (red) and daily mean (black) keel depth at M8.

Figure 10. Time series of (a) percent ice cover in the 50 km × 50 km box centered on M8, (b) color contours of daily averaged temperature at M8, and (c) color contours of the temperature anomalies at M8.

Figure 11. (a) Time series of monthly average temperature at M8 (2005-2017; blue) and MUR (2002-2017; orange). (b) Scatter plot of daily (gray) and monthly (blue) near surface temperature anomaly measured at M8 and SST from MUR. The trend line is through the monthly data. (c) Time series of MUR SST monthly mean anomalies. The colored lines at the bottom indicate periods of limited ice (red) and more extensive (blue) in December/January from Fig. 8.

Figure 12. (a) Daily average ice cover (NSIDC) in 50 km × 50 km box centered on M8 (1980–2017). The gray area indicates the SEM. (b) Daily average temperature at M8 (2005–2017) calculated using the data shown in Fig. 10b.

Figure 13. Monthly mean near-bottom temperature at M8 (color pixels) and indication of ice extent (white bars). The thin white lines indicate ice is present at >5% areal coverage and the thicker lines that ice is present at >80% areal coverage in the 50 km × 50 km box around M8. The black line at the bottom indicates the long term areal ice cover (>20%).

Figure 14. The annual signal of salinity at M8 (2005–2017) at 30 m (blue) and 55 m (orange). The salinity sensor at 55 m failed from September 2007 to August 2008, and the sensor at 30 m failed from September 2016 to August 2017.

Figure 15. Time series of monthly anomaly of salinity at M8 at 30 m (blue) and 55 m (orange). The shaded areas indicate December–February for each year.

Figure 16. Concentrations (µM) of individual samples of (a) nitrate, (b) silicic acid, and (c) ammonium in deep water (45–80 m) near the M8 mooring. The data are color coded by year as indicated in the symbol key for each year above the top panel.

Figure 17. Concentrations (µM) of (a) nitrate, (b) silicic acid, and (c) ammonium in shallow water (0–15 m) near the M8 mooring. The data are color coded by year as indicated in the symbol key above the top panel.

Figure 18. Time series of (a) phosphate, and (b) DIN concentrations (µM) in deep (60–80 m) water near the M8 mooring. Open circles include all samples collected regardless of season. Red circles are the yearly summertime means derived from the means of each summer cruise (July to mid-October) using only the deepest sample per cast. Error bars are the propagated standard deviations.

Figure 19. (a) The day of ice retreat (areal ice concentration is <20%) in 50 km × 50 km box centered at M8. (b) Abundance ($\log_{10}$ number m^{-3}) of different stages of *Calanus* spp. at M8 (70-km box). C1–C4 are early life-history stages.

Figures

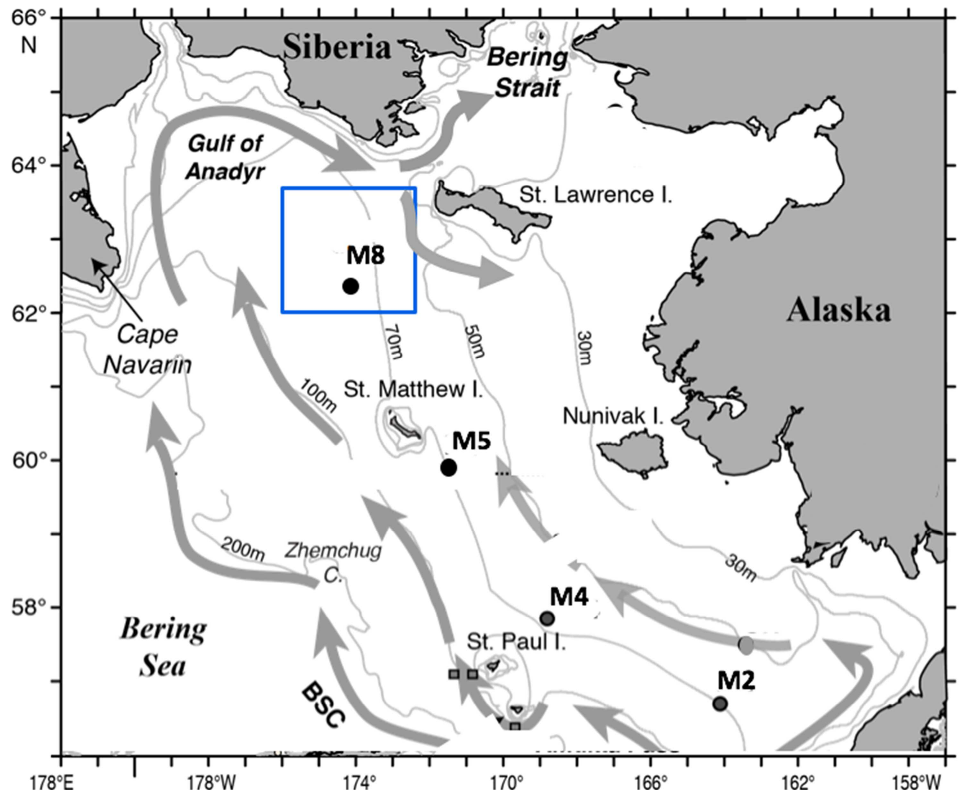

Figure 1. DBO-1 is indicated approximately by the blue box to the west of St. Lawrence Island. Mooring locations M2, M4, M5, and M8 are indicted. The flow patterns are adapted from Stabeno et al. (2017) and do not include the Alaskan Coastal Current nor the circulation around Pribilof Islands.

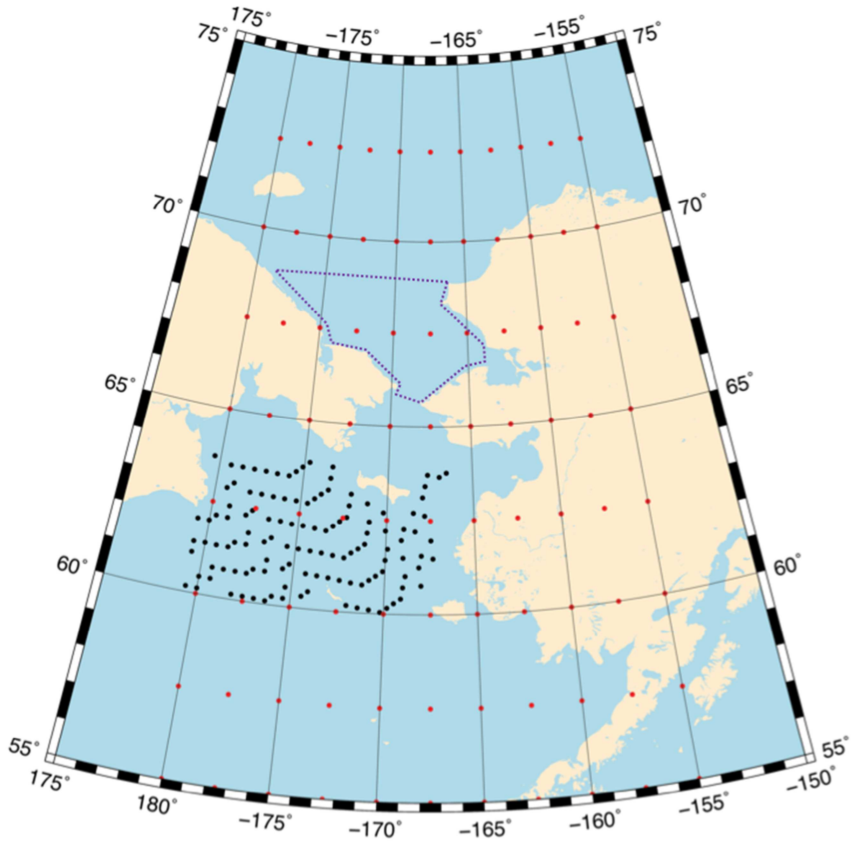

Figure 2. The sampling area for sea-ice concentration (black dots) and sea level pressure (red dots). The region in the Chukchi Sea where ice cover was calculated is outlined in purple.

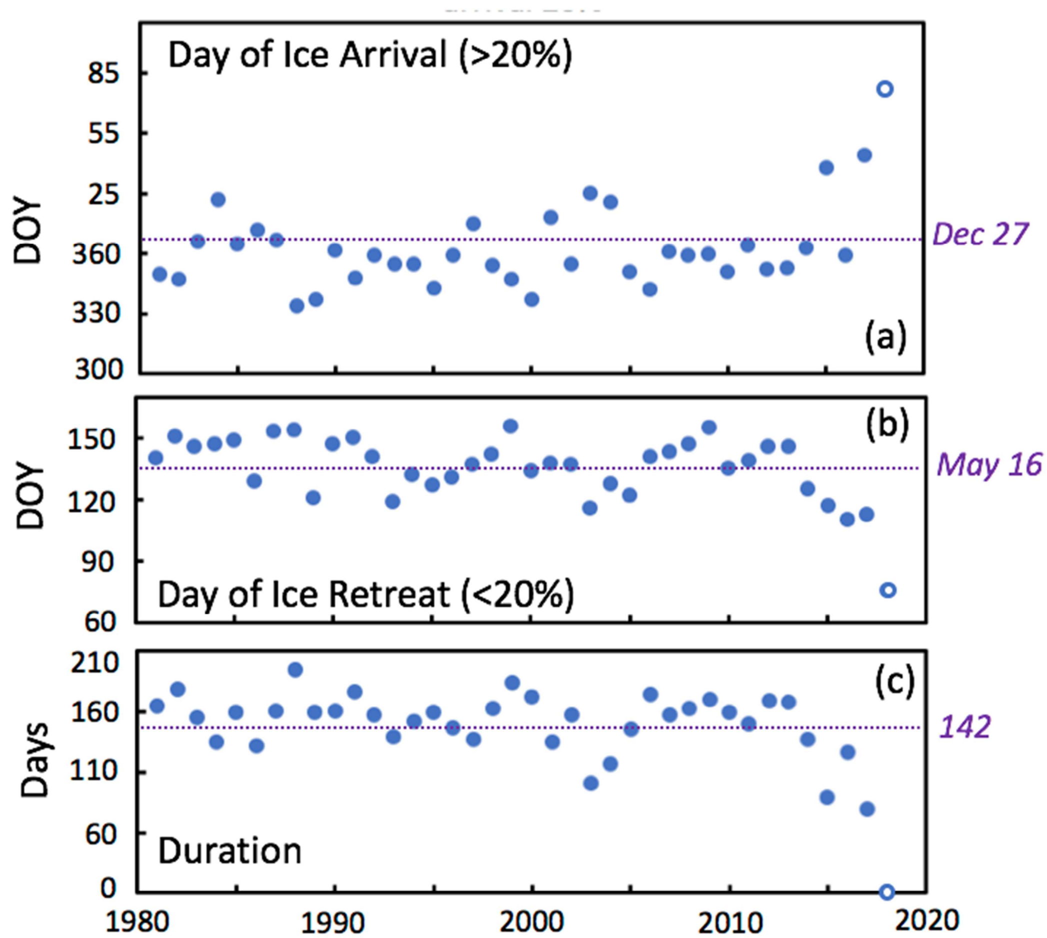

Figure 3. (a) Timing of the arrival (areal ice concentration >20%) of sea ice in the 50 km × 50 km box centered at M8. (b) The day of ice retreat (areal ice concentration is <20%). (c) The number of days between when ice arrives and departs the box around M8. The data points for 2017-2018 are open circles, indicating that these data are an interim product not the final bootstrap data product and that the estimated areal ice coverage is only 18%. In each panel, the dashed line indicates the mean of data set, excluding the 2018 data.

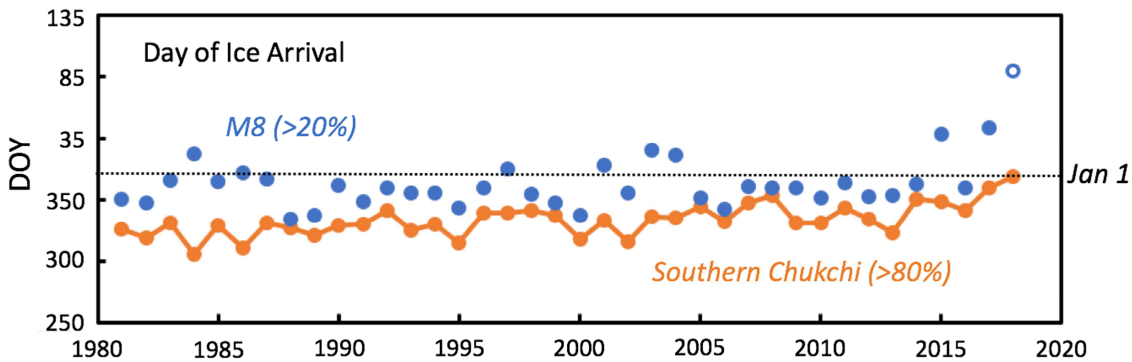

Figure 4. Time series of ice arrival 50 km × 50 km box centered at M8 (>20%) and the timing of 80% ice cover in southern Chukchi. Mean date at M8 of arrival is day 361 (27 December), and mean date for the southern Chukchi is day 332 (27 November). In 2018, sea-ice concentration only reached 18% at M8, which is indicated by the open circle.

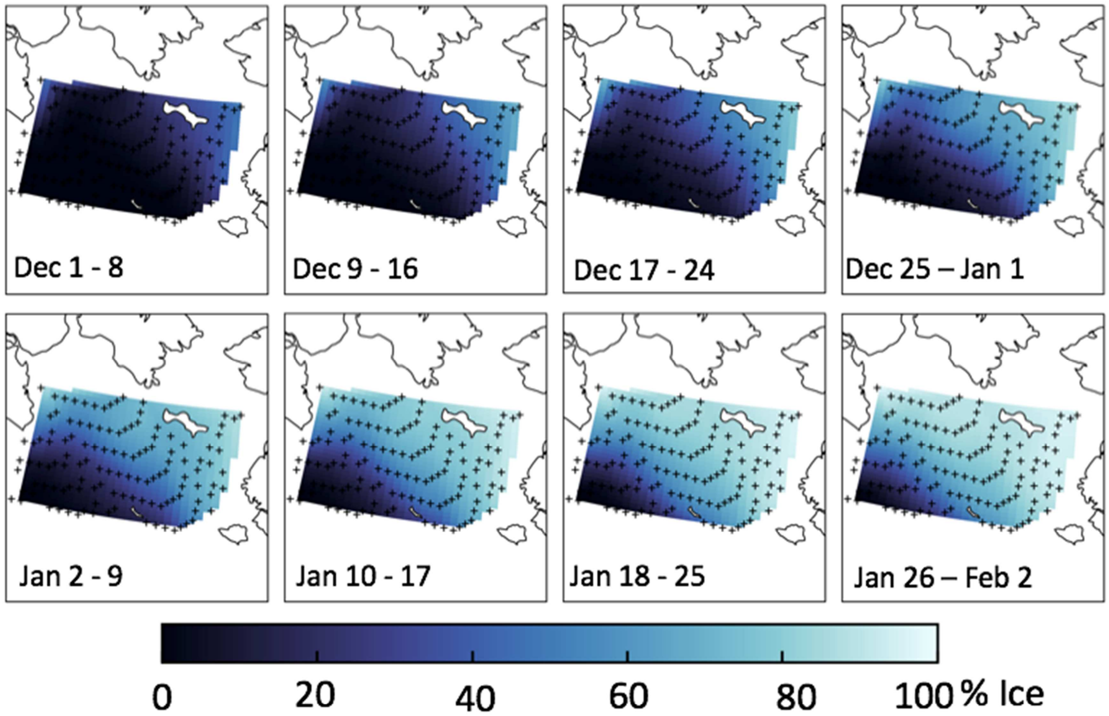

Figure 5. Patterns of average (1979–2017) ice cover in 8-day periods from December 1 through February 2.

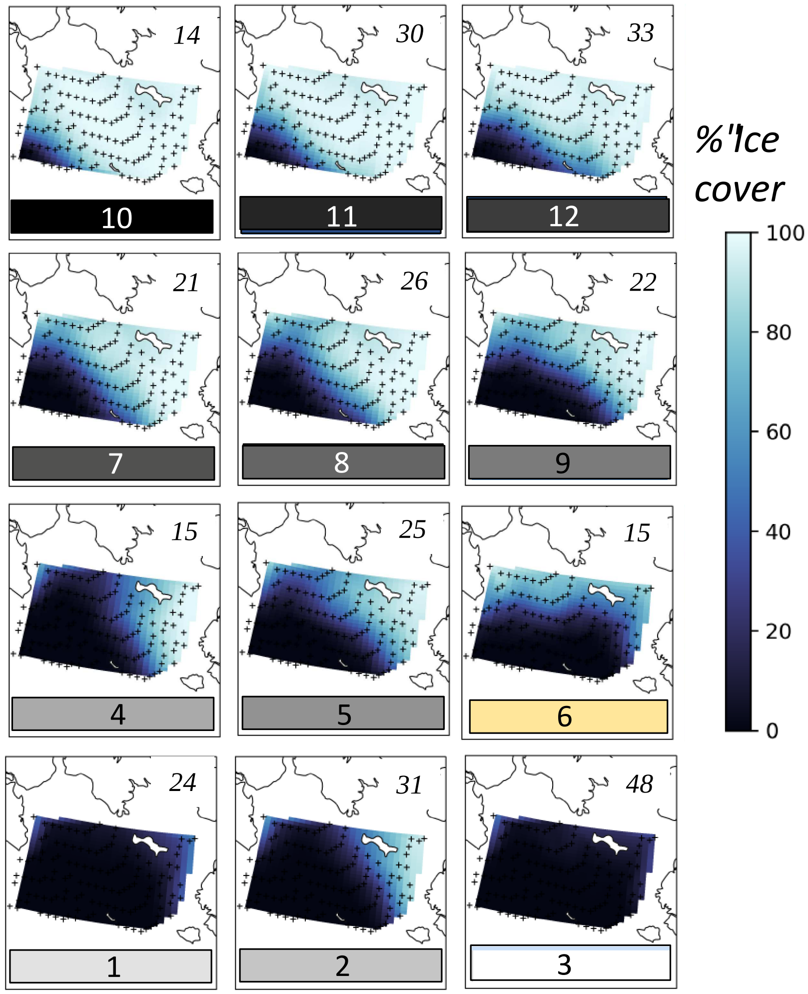

Figure 6. The 12, 8-day patterns of sea ice derived by SOM. The accompanying SLP patterns are shown in Fig. 7. The patterns are color coded in the lower part of each panel, from white (lowest ice concentration, pattern 3) to dark blue (highest ice concentration, pattern 10). Pattern 6 has the strongest north-south gradient. These color codes are used in Fig. 8. The numbers in the upper right-hand corners indicate the number of maps used in calculating that pattern.

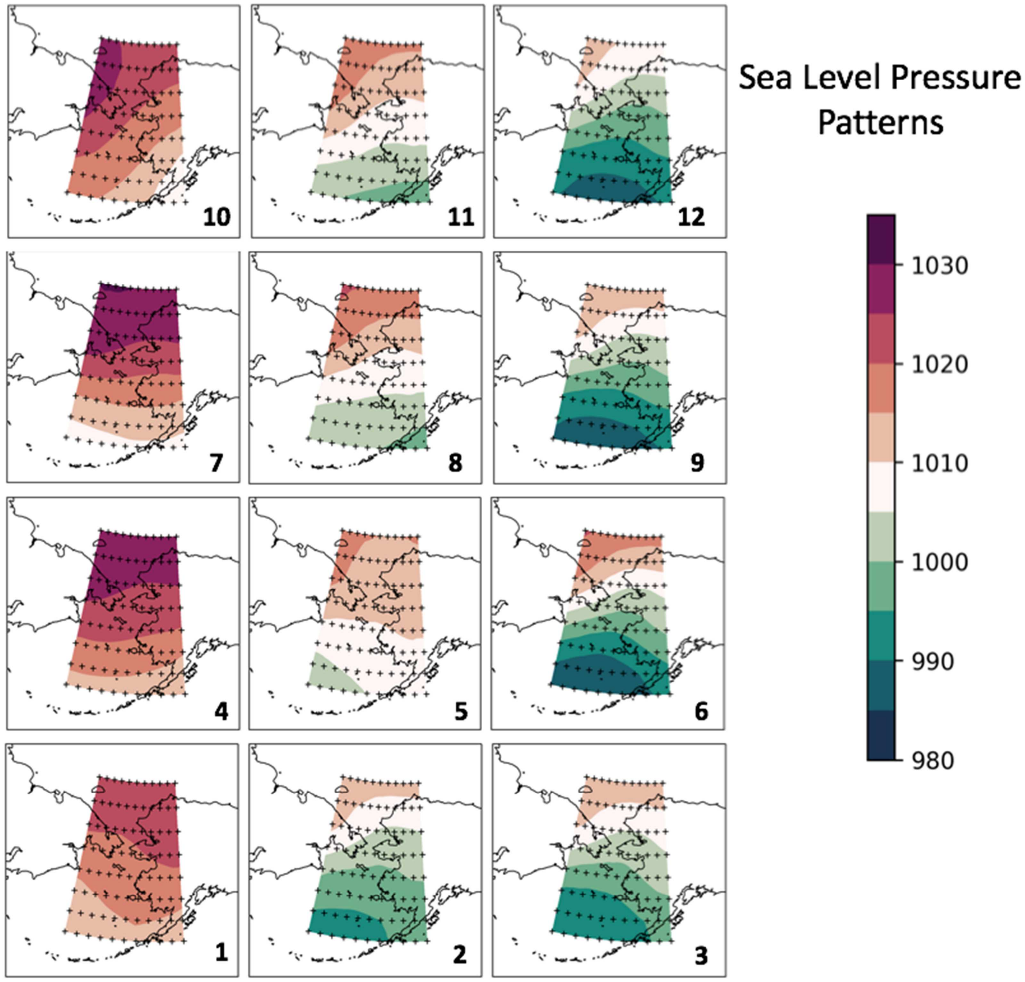

Figure 7. The 12, 8-day patterns of SLP calculated from SLPA derived by SOM. The number in the lower right-hand corner indicates the pattern number. The accompanying sea-ice patterns are shown in Fig. 6.

	December				January			
	1-8		17-24		2-9		18-25	
	1	**2**	**3**	**4**	**5**	**6**	**7**	**8**
1979-1980	3	2	4	9	8	7	11	11
1980-1981	3	4	4	7	11	12	12	12
1981-1982	2	5	8	9	4	7	7	8
1982-1983	2	2	2	9	8	7	8	12
1983-1984	3	3	1	1	1	2	5	7
1984-1985	3	3	3	1	6	6	6	6
1985-1986	3	3	3	3	6	9	8	8
1986-1987	3	3	3	6	9	9	9	12
1987-1988	5	3	3	3	3	9	12	8
1988-1989	5	8	12	12	12	12	11	11
1989-1990	2	2	2	4	8	12	12	11
1990-1991	1	2	5	5	7	7	11	11
1991-1992	1	3	2	9	12	12	12	11
1992-1993	2	9	8	8	5	5	12	11
1993-1994	3	2	9	9	9	7	7	11
1994-1995	5	5	12	12	12	12	12	10
1995-1996	1	1	2	9	9	7	7	7
1996-1997	1	2	2	4	4	4	8	7
1997-1998	3	2	5	8	7	7	11	11
1998-1999	3	6	2	4	7	7	12	11
1999-2000	5	8	10	11	10	10	10	12
2000-2001	3	3	3	3	3	6	9	6
2001-2002	2	5	8	12	11	12	11	10
2002-2003	3	3	3	3	5	9	5	8
2003-2004	3	3	2	2	2	4	4	7
2004-2005	3	3	6	5	1	5	7	9
2005-2006	4	8	8	12	12	11	10	10
2006-2007	3	3	2	9	12	8	11	11
2007-2008	3	3	1	5	8	11	11	11
2008-2009	2	4	5	5	10	10	11	10
2009-2010	2	5	8	9	8	11	12	11
2010-2011	1	1	1	4	8	8	7	11
2011-2012	2	2	9	12	11	11	10	10
2012-2013	1	4	5	8	12	12	11	10
2013-2014	1	1	1	5	5	9	12	12
2014-2015	1	3	3	3	1	1	2	5
2015-2016	3	3	3	6	6	6	6	6
2016-2017	3	1	1	3	3	1	2	2

Figure 8. Timeline of SOM patterns. Patterns are indicated by shades of gray and by the small number in each box. Note that the darker the color the more ice in the pattern. The yellow indicates pattern 6, with a strong north-south gradient. The warm (red) and cold (blue) years at the southern mooring, M2, are indicated on the right (data from Stabeno et al., 2017). The striped line indicates period of high year-to-year variability. The winter/spring of 2006 and 2017 had average ice cover, which is indicated by white.

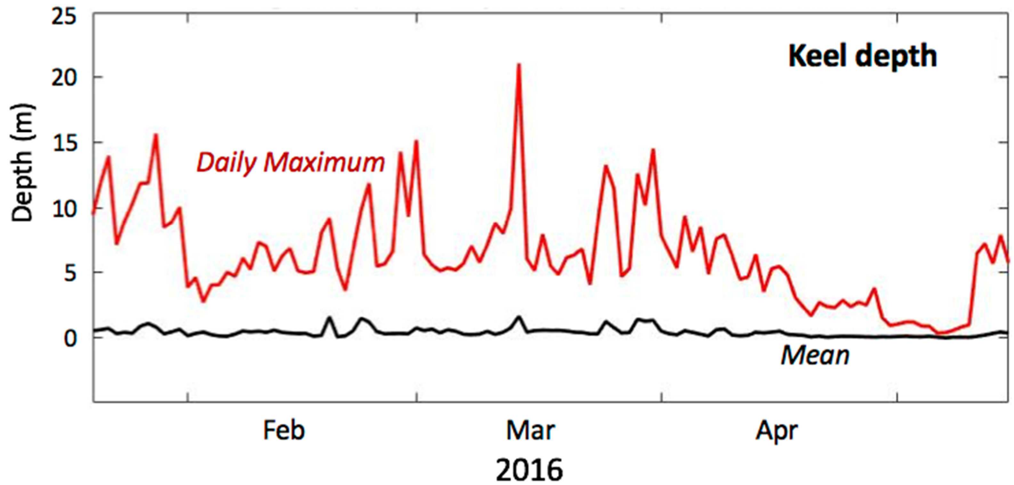

1072

1073

1074 **Figure 9.** Time series of daily maximum (red) and daily mean (black) keel depth at M8.

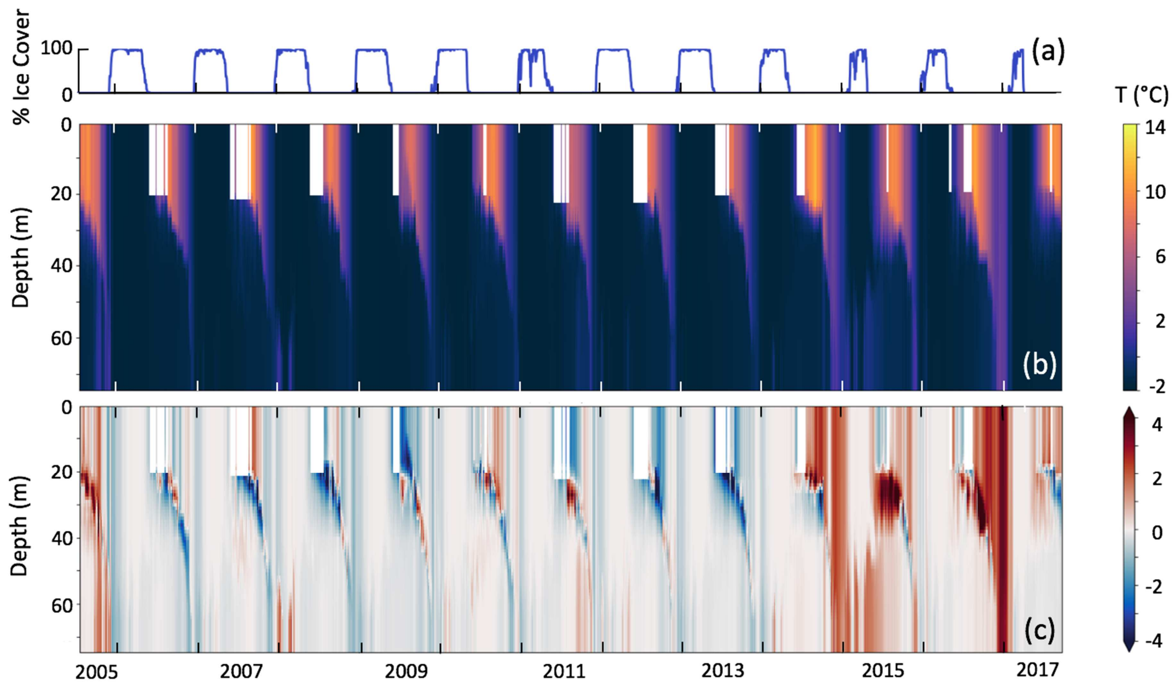

Figure 10. Time series of (a) percent ice cover in the 50 km × 50 km box centered on M8, (b) color contours of daily averaged temperature at M8, and (c) color contours of the temperature anomalies at M8.

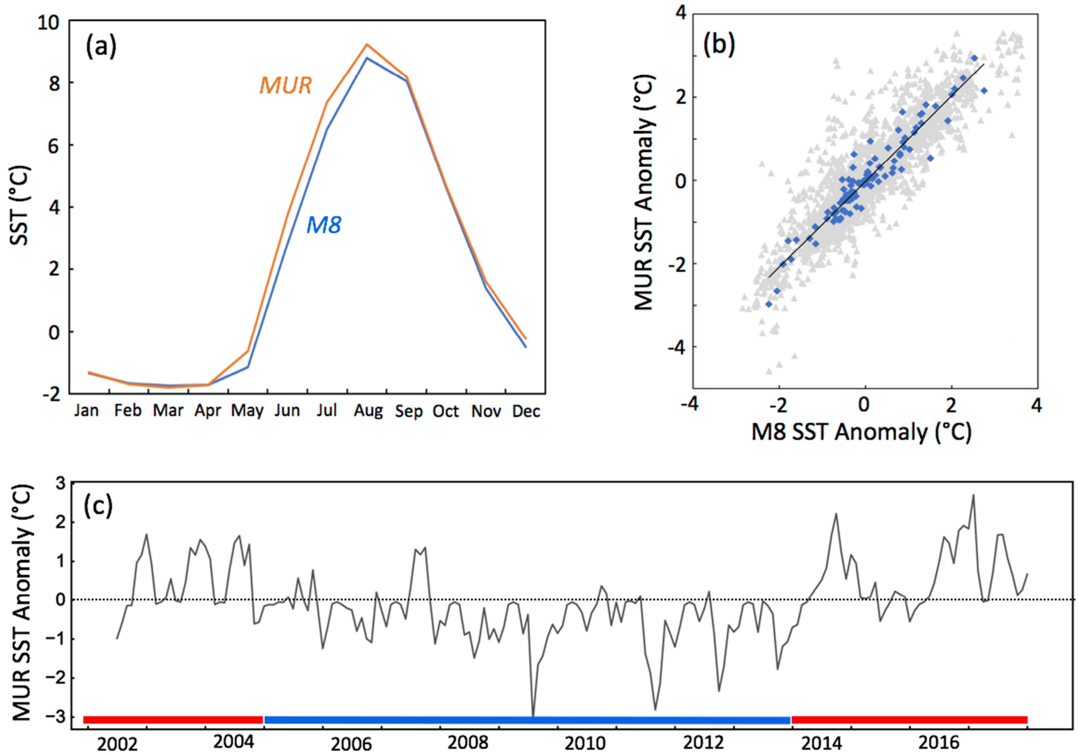

Figure 11. (a) Time series of monthly average temperature at M8 (2005-2017; blue) and MUR (2002-2017; orange). (b) Scatter plot of daily (gray) and monthly (blue) near surface temperature anomaly measured at M8 and SST from MUR. The trend line is through the monthly data. (c) Time series of MUR SST monthly mean anomalies. The colored lines at the bottom indicate periods of limited ice (red) and more extensive (blue) in December/January from Fig. 8.

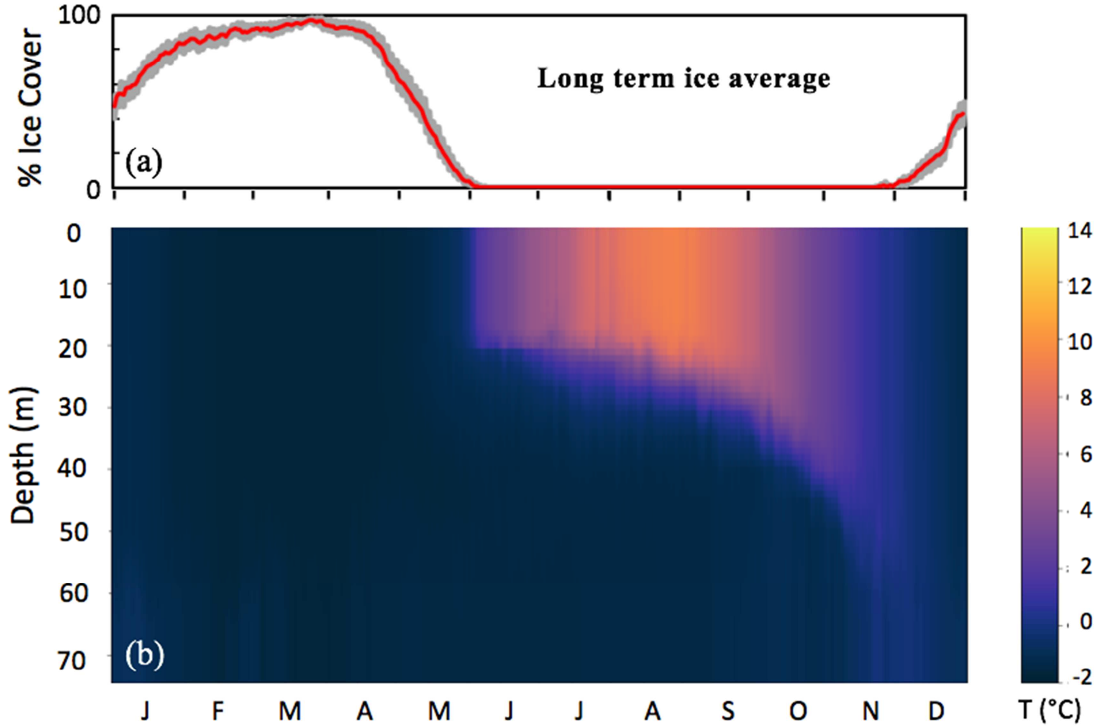

Figure 12. (a) Daily average ice cover (NSIDC) in 50 km × 50 km box centered on M8 (1980–2017). The gray area indicates the SEM. (b) Daily average temperature at M8 (2005–2017) calculated using the data shown in Fig. 10b.

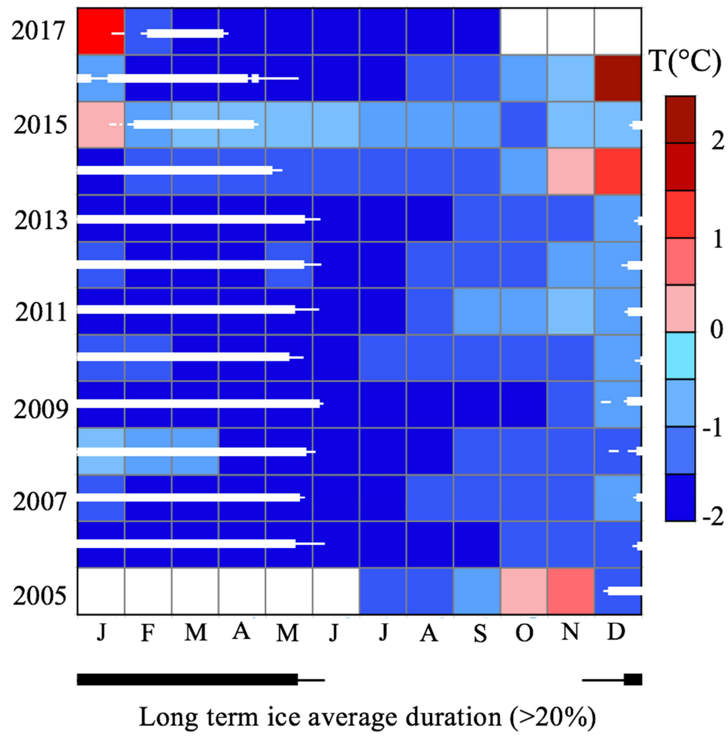

Figure 13. Monthly mean near-bottom temperature at M8 (color pixels) and indication of ice extent (white bars). The thin white lines indicate ice is present at >5% areal coverage and the thicker lines that ice is present at >80% areal coverage in the 50 km × 50 km box around M8. The black line at the bottom indicates the long term areal ice cover (>20%).

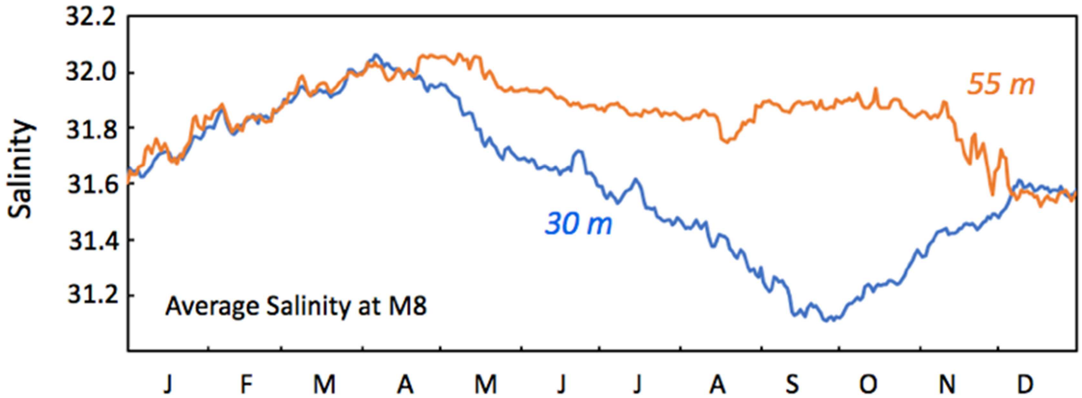

Figure 14. The annual signal of salinity at M8 (2005–2017) at 30 m (blue) and 55 m (orange). The salinity sensor at 55 m failed from September 2007 to August 2008, and the sensor at 30 m failed from September 2016 to August 2017.

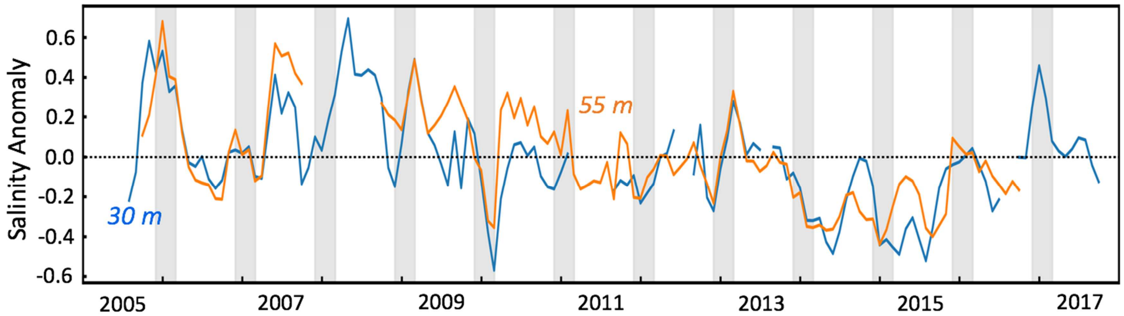

Figure 15. Time series of monthly anomaly of salinity at M8 at 30 m (blue) and 55 m (orange). The shaded areas indicate December–February for each year.

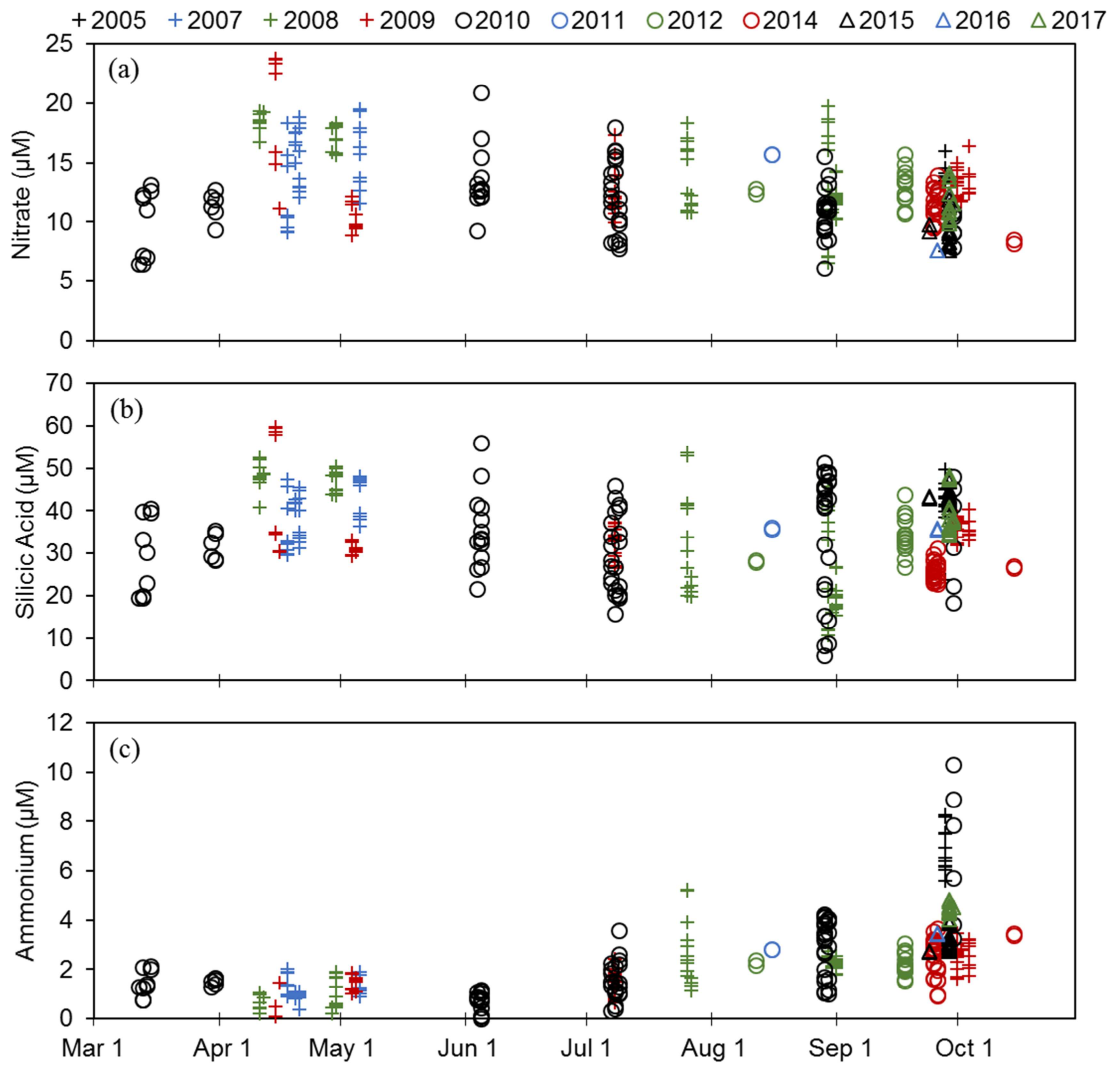

Figure 16. Concentrations (µM) of individual samples of (a) nitrate, (b) silicic acid, and (c) ammonium in deep water (45–80 m) near the M8 mooring. The data are color coded by year as indicated in the symbol key for each year above the top panel.

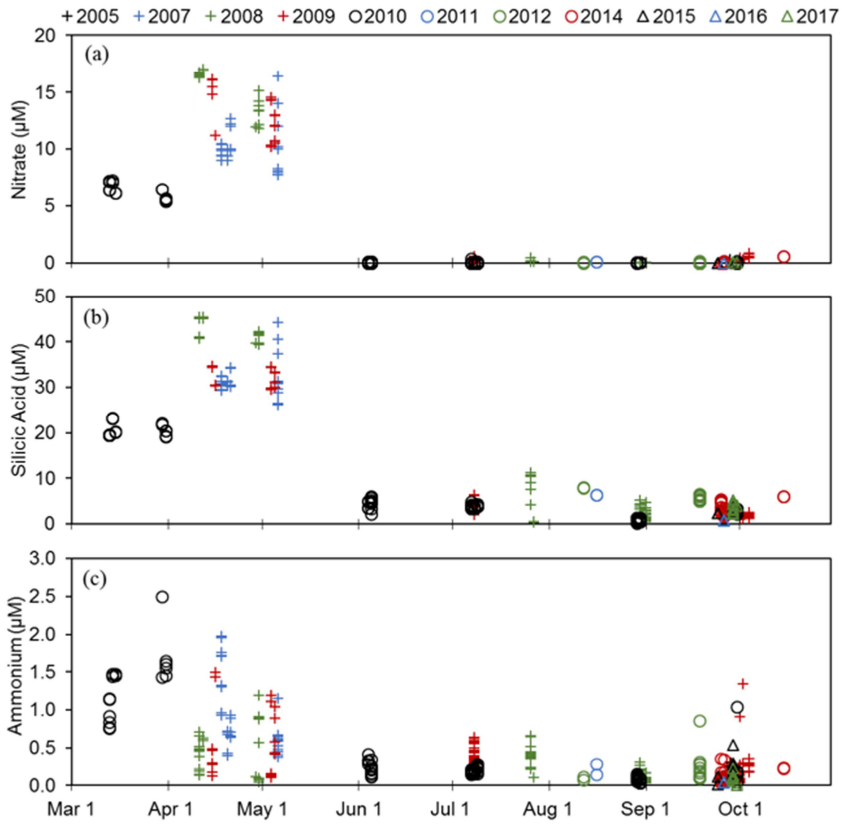

Figure 17. Concentrations (µM) of (a) nitrate, (b) silicic acid, and (c) ammonium in shallow water (0–15 m) near the M8 mooring. The data are color coded by year as indicated in the symbol key above the top panel.

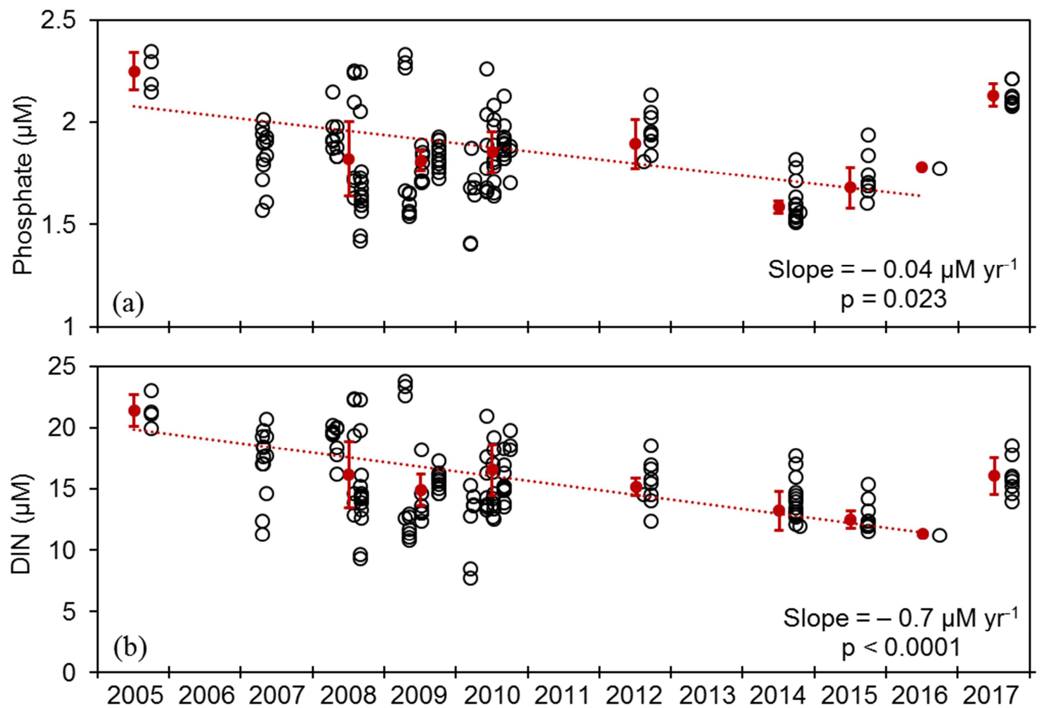

Figure 18. Time series of (a) phosphate, and (b) DIN concentrations (µM) in deep (60–80 m) water near the M8 mooring. Open circles include all samples collected regardless of season. Red circles are the yearly summertime means derived from the means of each summer cruise (July to mid-October) using only the deepest sample per cast. Error bars are the propagated standard deviations.

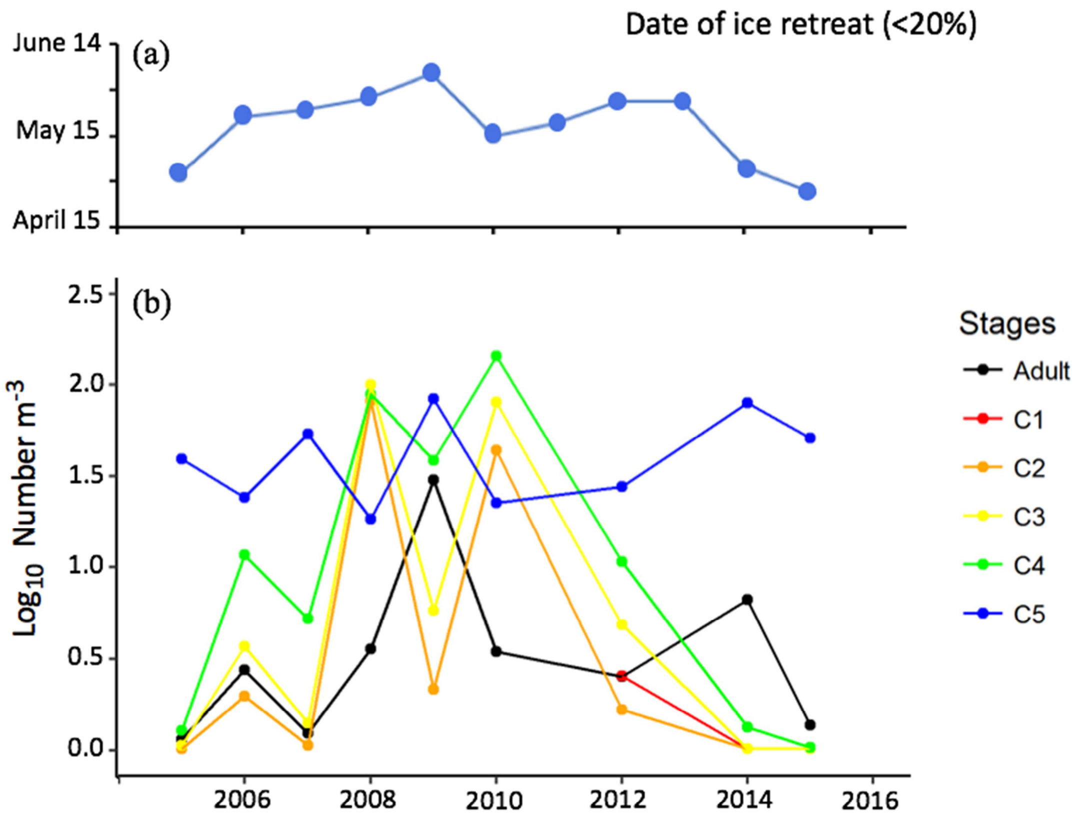

Figure 19. (a) The day of ice retreat (areal ice concentration is <20%) in 50 km × 50 km box centered at M8. (b) Abundance ($\log_{10}$ number m^{-3}) of different stages of *Calanus* spp. at M8 (70-km box). C1–C4 are early life-history stages.

Table S1. Hydrographic cruises between 2005 and 2017, which were used to collect nutrient samples in the upper (0–15 m) and lower (45–80 m) portions of the water column.

Year	Ship	PMEL Cruise ID	Number of Samples		Sampling Dates	
			0 - 15 m	45 - 60 m	Start	End
2005	NOAA Ship Miller Freeman	MF0513	4	12	9/28	9/28
2007	USCGC Healy	HLY0701	35	36	4/18	5/6
2008	USCGC Healy	HLY0802	25	25	4/11	4/30
	USCGC Healy	HLY0803	15	14	7/26	7/27
	R/V Melville	MEL0823	28	30	8/30	9/1
2009	USCGC Healy	HLY0902	22	22	4/15	5/5
	R/V Knorr	6N195J	22	17	7/8	7/8
	NOAA Ship Miller Freeman	MF0904L2	26	24	10/1	10/4
2010	USCGC Polar Sea	PSEA1001	17	15	3/12	3/31
	R/V Thompson	TN249	14	14	6/4	6/5
	R/V Thompson	TN250	24	22	7/7	7/9
	R/V Wecoma	WE1008	26	27	8/29	8/30
	NOAA Ship Miller Freeman	MF1006	6	6	9/30	9/30
2011	F/V Mystery Bay	MB1101	2	2	8/16	8/16
2012	F/V Aquilla	AQ1201	2	2	8/12	8/12
	NOAA Ship Oscar Dyson	DY1208	15	16	9/18	9/18
2014	NOAA Ship Oscar Dyson	DY1408L3	26	26	9/25	9/26
	F/V Aquilla	AQ1401L3	2	2	10/15	10/15
2015	F/V Aquilla	AQ1501	2	2	9/24	9/24
	NOAA Ship Oscar Dyson	DY1509	16	16	9/29	9/29
2016	F/V Aquilla	AQ1601	2	2	9/26	9/26
2017	NOAA Ship Oscar Dyson	DY1708	16	17	9/29	9/30